A Turbulence Survey in the Gulf of Naples, Mediterranean Sea, during the Seasonal Destratification

Florian Kokoszka, Fabio Conversano, Daniele Iudicone, Bruno Ferron, Pascale Bouruet-Aubertot

Journal of *Marine Science and Engineering*

MDPI

Article

A Turbulence Survey in the Gulf of Naples, Mediterranean Sea, during the Seasonal Destratification

Florian Kokoszka [1,*], Fabio Conversano [1], Daniele Iudicone [2], Bruno Ferron [3] and Pascale Bouruet-Aubertot [4]

[1] Department of Research Infrastructures for Marine Biological Resources (RIMAR), Stazione Zoologica Anton Dohrn, 80121 Naples, Italy
[2] Department of Integrative Marine Ecology (EMI), Stazione Zoologica Anton Dohrn, 80121 Naples, Italy
[3] Université de Brest, Centre National de la Recherche Scientifique (CNRS), Institut Français pour Recherche et l'Exploitation de la Mer (IFREMER), Institut de Recherche pour le Développement (IRD), Laboratoire d'Océanographie Physique et Spatiale (LOPS)—Institut Universitaire Européen de la Mer (IUEM), 29280 Plouzané, France
[4] Sorbonne Université, Centre National de la Recherche Scientifique (CNRS), Institut de Recherche pour le Développement (IRD), Muséum National d'Histoire Naturelle (MNHN), Laboratoire d'Océanographie et du Climat: Expérimentation et Approches Numérique (LOCEAN), 75005 Paris, France
* Correspondence: florian.kokoszka@szn.it

Abstract: The seasonality of the vertical mixing at coastal sites is not well characterized yet. Here, a time series of the dissipation rate of turbulent kinetic energy (ε) was obtained from weekly morning microstructure observations covering the destratification period (July 2015, February 2016) at a coastal site in the western Mediterranean Sea, influenced by freshwater runoffs. Estimated with bulk parameters from the public re-analyzed dataset ERA5, the Ekman layer, and the convective penetration depth scale with the mixed layer depth (*MLD*) with a good agreement. Below the *MLD*, peaks of ε are observed in the baroclinic layers that progressively overlap with the bottom layer, where repeated near-bottom turbidity peaks provide evidence of sediment resuspension, suggesting energetic processes within the bottom boundary layer. In the subsurface, moderate values (10^{-9} to 10^{-8} W kg^{-1}) are observed, following a Burr type XII distribution. Significant correlation with ε at *MLD* is obtained with a model combining the effects of wind, wind–wave, and convection, highlighting a calm sea bias in our data, plus a sunrise bias when morning buoyancy fluxes are stabilizing. Another correlation, obtained from a pure-wind estimation 18 h before, suggests the role of wind in generating internal waves in the stratified layers, thus, impacting mixing intensity.

Keywords: turbulence; Gulf of Naples; Mediterranean Sea; coastal boundaries; seasonal destratification; vertical mixing; dissipation rate; turbulent kinetic energy; mixed layer depth; microstructure observations

Citation: Kokoszka, F.; Conversano, F.; Iudicone, D.; Ferron, B.; Bouruet-Aubertot, P. A Turbulence Survey in the Gulf of Naples, Mediterranean Sea, during the Seasonal Destratification. *J. Mar. Sci. Eng.* **2023**, *11*, 499. https://doi.org/10.3390/jmse11030499

Academic Editor: Anatoly Gusev

Received: 26 January 2023
Revised: 14 February 2023
Accepted: 21 February 2023
Published: 25 February 2023

1. Introduction

The Gulf of Naples (GoN) is a coastal marine ecosystem in the western Mediterranean Sea (Figure 1) that features a subtropical regime, weak tides, and a marked salinity contrast due to the combination of salty Tyrrhenian Sea waters and freshwater inputs from a densely inhabited coastal area and nearby rivers [1,2]. It provides an ideal study site to understand how changes in coastal salinity and temperature affect vertical stratification [3], particularly in the context of rising air and sea temperatures and increased frequency of extreme events such as storms, floods, and Mediterranean hurricanes [4–6]. The GoN's inter-annual variability is influenced by a complex combination of temperature and salinity trends linked to large-scale atmospheric forcings on multi-annual scales [7].

However, the short-term impact of these forcings on the coastal system is not well understood. Levels of mixing caused by wind stress, waves, and buoyancy fluxes are still poorly observed in such boundary areas, where the proximity of the coast and the bottom possibly enhance some turbulent features [9]. Moreover, the presence of coastal

freshwater inputs can impact the stratification by straining the surface and subsurface density field [10,11], and possibly inhibiting small-scale mixing. As [12] suggest, the interactions between wind and waves through Langmuir circulation cells, as well as waves and sub-mesoscale filaments [13] in buoyant waters [14] may play a significant role in mixing the stratification in shallow enclosed areas such as the GoN, by enhancing the shear-driven turbulence [15] and/or adding its effect to the convective destabilizing events [16].

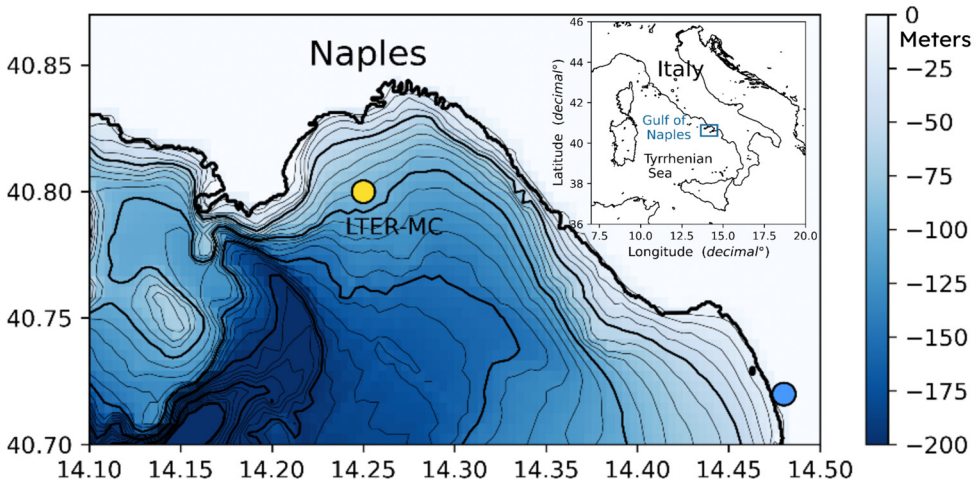

Figure 1. Bathymetry of the Gulf of Naples (GEBCO grid [8]) along the Tyrrhenian Sea in the western Mediterranean basin. The 75 m deep LTER-MC coastal sampling site (14.25 east, 40.80 north) is located by the yellow dot. Thin lines indicate isobaths every 10 m deep, and thick lines every 50 m. On the eastern part of the gulf, the Sarno river mouth is shown in blue.

These multiple forcings commonly act simultaneously in generating turbulence in the surface layer of the ocean and understanding their interplay is important for predicting the transport in the water column of scalars, momentum, and materials (e.g., plastics, plankton, sediments [17–19]), particularly in shallow coastal areas where turbulent structures can develop in the wavy Ekman layer [20] and extend over the full depth [21]. This could be of importance to the transport of negatively buoyant materials, such as the resuspension of sediment by the Langmuir turbulence in shallow seas [22,23].

The relative importance of wind, waves, and buoyancy fluxes on the vertical distribution of temperature and salinity varies greatly throughout the year, leading to a strong seasonality of fine-scale processes over the vertical dimension [24]. This seasonal variability also regulates the biological activity by controlling the vertical transfer and uptake of nutrients [25,26], and affects the behavior of marine species, taking advantage of or being limited by the water motions modulated by the stratification [27–29]. Understanding its seasonality in relation to mixing is, thus, relevant for the comprehension of biogeochemical cycles, harmful algae blooms, and plastic dispersal, among others [25,30,31].

Mixing observations have improved with high-resolution profilers since the 1960s [32–34], but the difficulty of deployment at sea and the complexity of physical phenomena cause in-situ characterization to be challenging. High-quality data collection at all scales, from open ocean to coastal area, remains of importance. Studies based on continuous detailed observations are crucial, as seen in recent works in lakes [35–37], which examine the impact of seasonal interactions between wind stress, internal waves, and convection on mixing in specific locations. Ultimately, time series observations of mixing (intensity, location, and intermittency) are important for improving the predictions of numerical simulations [38,39]. In this context, our observations contribute to the Long-Term Ecosystem Research Marechiara (LTER-MC) initiative that produced a historical time series of a Mediterranean coastal ecosystem through weekly sampling of the water column starting in 1984 and running until now [7,40,41].

With a time series of microstructure observations, we will examine the hydrological and turbulence features in a shallow coastal area of the GoN during the seasonal destratifica-

tion period from July 2015 to February 2016 (Section 3.1). We will analyze the atmospheric context of wind stress, waves, and buoyancy fluxes, and relate the *MLD* deepening to these forcings, by comparing the *MLD* to vertical scales that model the penetration due to wind friction and convection (Section 3.2). Our analysis will provide a framework for characterizing the turbulent environment in the GoN by layers and periods of forcings (Section 3.3). Finally, we will test a model estimating dissipation rates associated with wind, wind–wave, and convection (Section 3.4), and use this information to establish a seasonal cycle for dissipation that can be used to extend time series when in-situ observations are not available.

2. Materials and Methods

2.1. Geographical Situation and Collected Data

The measurement campaign took place in the Gulf of Naples (GoN)—a coastal bay located in the Mediterranean Sea (Figure 1). The GoN has a sub-tropical climate and low tides, and its bathymetry is generally gentle and regular in the eastern half. It is bordered by several mountain systems (e.g., Mount Vesuvius to the northeast, the Lattari Mountains on the Sorrentine Peninsula to the east and southeast) and the river Sarno flows through the region. In contrast, the western half of the GoN is more rugged and includes several deep submarine canyons (e.g., Canyon Dohrn, Bocca Grande) that extend from the islands of Capri in the south to Ischia in the west. The Marechiara (MC) coastal reference point, located 2 km from the coast at a depth of 75 m, has been used for over 30 years as a monitoring site within the framework of the national long-term ecological research network (LTER-MC).

Hydrology and turbulence data were collected weekly at the Marechiara point using a vertical microstructure profiler (VMP-250) manufactured by Rockland Scientific International (RSI) from July 2015 to March 2016. One to four vertical profiles were collected per trip, usually between 8:00 and 10:00 am (Table 1). The profiler was deployed from the surface and made a free descent in the water column at a vertical speed of 0.7–0.9 m s^{-1}. The instrument was tethered with a low hydrodynamic drag cable. Sufficient slack was provided during the descent to avoid contamination of the signal by vibrations. The VMP was equipped with two perpendicularly oriented microstructure shear sensors (SH1, SH2), a fast response thermistor (FP07), a micro-conductivity sensor (SBE7), and JFE Advantech optical sensors for measuring fluorescence (FLUO) and turbidity (TURB) in the water column. All of these sensors were sampled at 512 Hz, except for the 64 Hz JFE-CT sensors. The VMP-250 data were processed using the Matlab ODAS Toolbox provided by RSI (v4.5.1). A total of 71 profiles were collected over 31 unique days distributed weekly from summer to winter. This measurement campaign was conducted as part of the LTER-MC program, which uses a Seabird 911+ CTD (conductivity, temperature, depth) probe mounted on a rosette with 12 Niskin bottles to collect water samples for bio-geochemical analyses. The microstructure profiles were generally collected on the same day as the CTD deployment, with a few exceptions where a special trip was dedicated the day before or after. The time period covered (July 2015 to March 2016) corresponds to stations MC1160 to MC1190 (as described in [7]).

2.2. Microstructure, Dissipation (ε), and Diffusion (κ) Rates of Turbulent Kinetic Energy (TKE)

The shear probes (SH_1, SH_2) measured the vertical shear of horizontal velocity fluctuations (i.e., $\frac{\partial u}{\partial z}$, $\frac{\partial v}{\partial z}$). The raw signals are subject to noise and signal contamination from instrument vibrations, internal circuitry, and impact of biology and sediments. To reduce the impact of signal contamination, several processing steps were required before computing the shear spectra and dissipation rate. Firstly, the upper and lower meters of each cast, where the profiler was stopped, were identified and discarded manually. Secondly, spikes of large-amplitude and short-duration were eliminated from the shear data using the de-spiking algorithm provided in Rockland's ODAS Matlab Library. In particular, spikes were identified using a threshold value of 8 when comparing the instantaneous

shear signal to a smoothed version. The smoothed signal was obtained using a first-order Butterworth filter, with a cut-off frequency ranging from 0.7 to 0.9 Hz, depending on the median value of the fall speed. Once identified, spikes were removed over a 5 cm segment (ca. 0.07 s). Thirdly, the shear signals were high-pass filtered at 1.5 Hz to remove low-frequency contamination (0.1–1.0 Hz) possibly associated with the pyroelectric effect [42] and low frequency vibrations induced by the moving VMP [43]. The spectrum of the high-passed vertical shear signal was computed and used to estimate the dissipation rate. The dissipation rate of turbulent kinetic energy (TKE) was calculated using the isotropic relation $\varepsilon = 7.5\ \nu < \left(\frac{\partial u}{\partial z}\right)^2 >= 7.5\ \nu < \left(\frac{\partial v}{\partial z}\right)^2 >$, where ν is the kinematic viscosity of seawater and u and v are the horizontal components of the small-scale velocity fluctuations. In practice, the estimate of ϵ was obtained iteratively by integrating the velocity shear spectrum $\phi(k)$ up to an upper wavenumber limit (k^{max}), i.e., $\varepsilon = 7.5\ \nu \int_0^{k^{max}} \phi(k)\ dk$ as it is outlined in Rockland's technical note 028 [44]. This was performed for each microstructure sensor separately, i.e., for $\frac{\partial u}{\partial z}$ (SH_1) and $\frac{\partial v}{\partial z}$ (SH_2). Dissipation segment lengths of 6 s were used with 2 s FFT segments that overlapped by 50%. The dissipation segments themselves were overlapped by ca. 1.5 s, which resulted in a vertical resolution in ε of approximately 4 m (values are later interpolated linearly on a 1 m regular vertical grid). Contamination of the spectra for instrument vibrations was reduced using the cross-coherency method of [45]. The last release of ODAS (v.4.5.1, June 2022) includes a correction to the Goodman routine to remove biases in the dissipation rate [43,46]. The quality of the spectra were assessed using a figure of merit, which is defined as $FM = \sqrt{DOF} \cdot MAD$, where $DOF = 9.5$ is the number of degrees of freedom of the spectra [47] and MAD is the mean absolute deviation of the spectral values from the Nasmyth spectrum as $MAD = \frac{1}{n_k} \sum_{i=1}^{n_k} \left| \frac{\phi(k_i)}{\phi_{Nasmyth}(k_i)} - 1 \right|$ where n_k is the number of discrete wavenumbers up to k^{max} [48]. Segments of data where the spectra had $FM > 1.5$ were rejected from further analysis. The final dissipation rate was obtained by averaging the estimates for the two independent probes, i.e., ε_{SH1} and ε_{SH2}. If their values differ by more than a factor of 10, the minimum value is used. Finally, surface values above 10^{-5} W kg^{-1} were removed (e.g., ship wake) and we did not consider the first 5 m in our statistics.

2.3. Turbulent Activity Index

The turbulent activity [49,50] is quantified by the buoyancy Reynolds number Re_b derived from the ratio between the Ozmidov scale $L_O = (\varepsilon\ /\ N^3)^{1/2}$ and the Kolmogorov scale $L_K = (\nu^3/\ \varepsilon\ )^{1/4}$, with $Re_b = \left(L_O\ /\ L_K\right)^{4/3} = \varepsilon\ /\ (\nu N^2)$ where ν is the kinematic viscosity. The buoyancy Reynolds number can be interpreted as the ratio of the maximum length at which eddies can overturn before being inhibited by buoyancy to the length scale at which the smallest eddies are eroded by viscous forces [51]. The study of [52] indicates that fully turbulent isotropic mixing takes place for $Re_b > 100$, while a transitional regime occurs for $7 < Re_b < 100$ in which turbulence is not fully isotropic but able to mix the stratification. In general, a turbulent activity index lower than [7.0–20.0] should indicate quiescent flow driven by molecular and buoyancy-controlled regimes, which is not turbulent enough to generate an important diapycnal mixing [53,54].

2.4. Hydrology

The hydrological temperature and salinity were derived from the calibrated JFE-CT sensor. Consistent vertical profiles were obtained by averaging the raw data on a regular vertical grid of 10 cm, using a vertical binning dependent on the median profiling velocity. Given the sampling rate and a speed of 0.7 m s^{-1}, ensembles of nearly 92 data points are used to provide averages every 10 cm. We used the Gibbs–SeaWater Oceanographic Toolbox [55] to calculate the conservative temperature θ (°C), the absolute salinity A_S (g kg^{-1}), the water density anomaly ρ (kg m^{-3}), the potential density σ_0 (kg m^{-3}), the potential temperature θ_0 (°C), and the Brunt–Väisälä frequency N^2 (s^{-2}). When mentioned thereafter, T and S refer to θ and A_S.

Table 1. Dates and time (local time = UTC + 1) of each VMP cast, with the number N of profiles created, and the LTER-MC reference number (cells are left blank when the VMP cast was not performed on the same day as the MC cast).

Cast	Date	Time	N	MC	Cast	Date	Time	N	MC
1	7 July 2015	07:58	2	1160	17	27 October 2015	09:33	2	1175
2	15 July 2015	09:38	2		18	3 November 2015	09:28	2	1176
3	21 July 2015	08:04	4	1162	19	10 November 2015	09:24	2	1177
4	28 July 2015	08:18	4	1163	20	18 November 2015	09:21	2	1178
5	4 August 2015	07:48	4	1164	21	24 November 2015	09:48	2	1179
6	11 August 2015	08:11	2	1165	22	1 December 2015	09:08	2	1180
7	18 August 2015	07:55	2	1166	23	9 December 2015	09:27	2	1181
8	26 August 2015	07:34	4		24	15 December 2015	09:31	2	1182
9	1 September 2015	07:43	4	1168	25	22 December 2015	09:01	2	1183
10	8 September 2015	07:57	2		26	29 December 2015	09:00	2	1184
11	10 September 2015	08:46	1	1169	27	19 January 2016	08:36	2	1186
12	16 September 2015	08:26	4	1170	28	26 January 2016	09:58	2	1187
13	22 September 2015	07:55	4	1171	29	2 February 2016	11:29	2	1188
14	8 October 2015	08:37	2	1172	30	18 February 2016	08:37	2	1189
15	13 October 2015	08:21	2	1173	31	23 February 2016	10:19	2	1190
16	22 October 2015	08:09	2	1174					

2.5. Optical Sensors

The fluorometer-turbidity sensor from JFE Advantech has a spatial response of ca. 1 cm [56] and the data were bin-averaged on a regular grid of 10 cm following the same procedure as for the JFE-CT. Given the 512 Hz sampling rate with a speed of 0.7 m s^{-1}, ensembles of nearly 733 data points were averaged per bin. Data were preliminarily despiked, applying the same settings as for microstructure shears. For turbidity (FTU, Formazin Turbidity Units), we offset down each profile from its minimum value. Some diverging values (>100) were removed. The obtained profile was then smoothed using a 5 m running median. Some profiles were discarded and eventual missing segments in the individual profiles due to the data cleaning are solved when averaging all the profiles of the same cast to produce one unique daily profile.

2.6. Atmospheric Forcings from Bulk Parameters

Surface heat fluxes, wind velocities (u_{10}, v_{10}), evaporation and precipitation rates (E, P), and significant wave height (H_S) were extracted from the ERA5 re-analysed product provided by Copernicus [57] to estimate buoyancy fluxes at the air–sea interface, wind friction, and Langmuir number at the sea surface for the area surrounding the coastal monitoring point. The buoyancy flux B_0 (m^2 s^{-3} or W kg^{-1}) is defined negatively when stabilizing the water column and is proportional to the density flux at the surface, as $B_0 = g\,\frac{Q_p}{\rho_0}$, where the density flux Q_p into the ocean from the atmosphere was computed as $Q_p = \rho(\alpha F_T + \beta F_S)$ [58], with α and β the thermal expansion and saline contraction coefficients, respectively. Here, $F_T = -(Q_{net}/\rho_{sea})C_p$ and $F_S = (E - P)S/(1 - S/1000)$, where C_p is the specific heat of seawater and S the sea surface salinity. The net radiative heat flux at the ocean surface Q_{net} (W m^{-2}) was calculated from the combination of the incoming short wave, net incoming and emitted long wave, and sensible and latent heat. The velocity friction u_* was calculated as $u_* = \sqrt{\tau\ /\ \rho_{sea}}$, where ρ_{sea} is the density of seawater, and τ the wind stress, as $\tau = \rho_{air} C_D U_{10}^2$, where $\rho_{air} = 1.22$ kg m^{-3}. The drag coefficient, C_D, and velocity at 10 m, U_{10}, were calculated from the wind velocity following [59]. To

include the effect of waves, we calculated the Langmuir number La [60] that relies on the interaction between the Stokes drift and the wind-forced surface shear. Under favorable conditions between wind and sea state, the wave field can generate vertically aligned Langmuir circulations cells [61] that can contribute significantly to the mixing in the surface layers. The Langmuir number is defined as $La = \sqrt{u_* \,/\, u_S}$, where u_S is the Stokes drift velocity, and La is considered to be critical for wave dominance when its values are close and below to 0.5 [62]. Stokes drift was estimated from bulk values of wind velocity and sea wave [63,64]: $u_{Stokes} = 5 \cdot 10^{-4}(1.25 - 0.25\left(0.5/f_c\right)^{1/3}\right)W_{10}W_{10}^{m} + 0.025(H_s - 0.4)$, where $f_c = 0.5$ Hz refers to the cut-off frequency, and W_{10}^{m} is an upper threshold for the wind module ($W_{10}^{m} = W_{10}$ if $W_{10} < 14.5$ m s^{-1}, $W_{10}^{\mathrm{m}} = 14.5$ if $W_{10} > 14.5$ m s^{-1}), and H_s is the significant wave height. Values $H_s < 0.4$ were not considered in the estimation and we considered $u_S = 0$ and $La = \infty$. To bring insights about the influence of freshwater runoffs from the land in the area, we use the river discharge and related historical data from the European Flood Awareness System provided by Copernicus (https://cds.climate.copernicus.eu/cdsapp#!/dataset/efas-historical?tab=overview, accessed on 6 July 2022). This dataset provides gridded modeled sub-daily and daily hydrological time series forced with meteorological observations. The dataset is a consistent representation of the most important hydrological variables across the European Flood Awareness System (EFAS) domain. We use the daily river discharge (m^3 s^{-1}) during the last 24 h, around the GoN area, and we identify the Sarno river as the dominant contributor (average flow of 10 m^3 s^{-1}, compared to 2.0–3.0 m^3 s^{-1} for Napoli or Bagnoli rivers). Note that the Sarno average is coherent with the 13 m^3 s^{-1} flow mentioned in [65].

2.7. Mixed Layer Depth

We estimated the mixed layer depth (MLD, m) with the method of [66] based on threshold values. Given a vertical profile of density $\sigma_0(z)$, or potential temperature $\theta_0(z)$, we calculated the depth below $z_{ref} = 3$ m where the profile reached various thresholds, defined as cumulative of 0.2 °C for θ_0, and 0.05 and 0.15 kg m^{-3} for σ_0. Due to the salty subsurface layers observed during some casts, the density-based estimate using a threshold of 0.05 kg m^{-3} was sometimes too shallow when compared to the visual MLD that was closer to the temperature-based estimate. To detect such a case and automatize the procedure, we used at the same time another density-based estimate with a stronger threshold of 0.15 kg m^{-3}. If the first estimate (threshold of 0.05 kg m^{-3}) was shallower than the temperature-based estimate (threshold of 0.2 °C), the second one (threshold of 0.15 kg m^{-3}) was used to replace the first one.

2.8. Baroclinic Layers

We hypothetize that internal wave breaking is among one of the processes that lead to intensified dissipation rates, and we propose to identify the stratified layers below the MLD where the maxima of the main baroclinic modes are located. We presume these layers could contain most of the energy of the internal oscillations. Ocean dynamic vertical modes were calculated for each profile from N^2, using the routine from [67]. Profiles were smoothed by filtering over a 10 m length running window before applying the algorithm. We focused on the first two modes (BC_1 and BC_2) that presented the largest variances. For each profile we identify the depth where the shear associated to each mode was maximum. We considered only the stratified part of the water column and we conserved the depths located below the MLD. The maxima of BC_1 are located below the MLD and are associated with the highly stratified part of the water column, while the maxima of BC_2 lie deeper and are associated with a weaker stratification.

2.9. Ekman Layer and Convection Depth: A Scaling of the Combination of Wind and Buoyancy Effects

To represent the influence of the wind stress u_* and rotation f on the mixed-layer deepening, the stratified Ekman scale is calculated to be compared to the MLD. We follow the

parametrization of [68] that defined $L_E = 1.9\, u_* / \sqrt{fN}$ where N is the buoyancy frequency from in-situ profiles that have been averaged over the MLD before being interpolated linearly on the ERA5 timestamp. Noteworthy, the authors consider the wind stress 12 h in advance of the observations to account for the adjustment time of inertial oscillations to produce critical shear at the base of the mixed layer. In our time series we will consider L_E during the last 18 h before the MLD observation. To represent the thermal convection due to the buoyancy fluxes applied at the sea surface, we follow [69] and apply the case of pure buoyancy fluxes to provide a scaling for the non-penetrative deepening of a mixed layer, as $\delta_C = N^{-1}\sqrt{2B_0\delta t}$ where δt is the duration (here $\delta t = 1$ h) to estimate a shallowing or deepening rate (in m h^{-1}), due to stabilizing or destabilizing convection. This is a good approximation for our observations since it happens during the night. We combine L_E and δ_C to scale the MLD in the preceding 18 h as: $L_{EC} = L_E + \sum_{cumul.t=-18}^{t=0} \delta_C$.

2.10. A Model for ε

Taking into account the direct contribution of buoyancy and mechanical mixing at the air–sea interface to the evolution of the ocean surface boundary layer (OSBL), ref. [62] derived a parameterization (mentioned thereafter as B12) for ε as the result of a linear combination of wind stress, wave–wind interaction through the Langmuir circulation cells, and buoyancy forcing due to destabilizing convection, valid at the depth where the three forms of turbulence are considered to be well established. This formulation derives from a universal function using the mixing or mixed layer length scale h, the cubic wind friction u_*^3, the Langmuir number La, the convection velocity scale $w_* = (B_0 h)^{1/3}$, and the velocity scale for wave-forced turbulence $w_{*L} = (u_*^2 u_s)^{1/3}$. Dissipation rates are given by the linear combination of the effect of wind, wave, and convection at the depth h, as $\varepsilon_{B12} = \varepsilon_{wind} + \varepsilon_{wind-wave} + \varepsilon_{conv} = E_S u_*^3/h + E_L w_{*L}^3/h + E_C w_*^3/h$, with $E_S = 2\left(1 - e^{-La/2}\right)$, $E_L = 0.22$ [70], $E_C = 0.3$ [71]. The authors pointed to the fact that warming at the ocean surface would re-stratify the ocean surface boundary layer and inhibit the turbulent mixing, and this case was not considered by the authors. In our study, it can happen during the diurnal cycle when B_0 changes its sign due to stable fluxes (with our definition, $B_0 < 0$), and in this case, values of the convection term are not considered, and the term is taken equal to zero. The comparisons with the observations are evaluated at the MLD.

2.11. Definition of the Statistics Used in this Study

When several consecutive casts were performed, they were averaged to produce the daily representative vertical profile (Table 1). The monthly average is the mean of the parameter values for each month of the year. Linear regressions and statistics were performed using the "linregress" function from the Python library scipy.stats [72], peaks were identified using the "find_peaks" function, probability distributions functions (PDF) and boxplots were calculated using the "hist" and "boxplot" functions (minimum, first quartile, median, third quartile, maximum), and the Burr XII distribution [73] fit with its parameters were obtained using the "burr12" function. The fitting of probability distributions to data was performed with the Python package (https://fitter.readthedocs.io/en/latest/, accessed on 6 July 2022).

3. Results

3.1. Hydrological and Turbulence Observations

We present the hydrological and microstructure observations that were performed between July 2015 and February 2016, following the seasonal destratification of the water column marked by a deepening MLD. We show in Figure 2 the vertical profiles of the water column, for (a) salinity, (b) temperature, (c) turbidity, (d) dissipation, (e) diffusion rates of turbulent kinetic energy, and (f) the buoyancy Reynolds number.

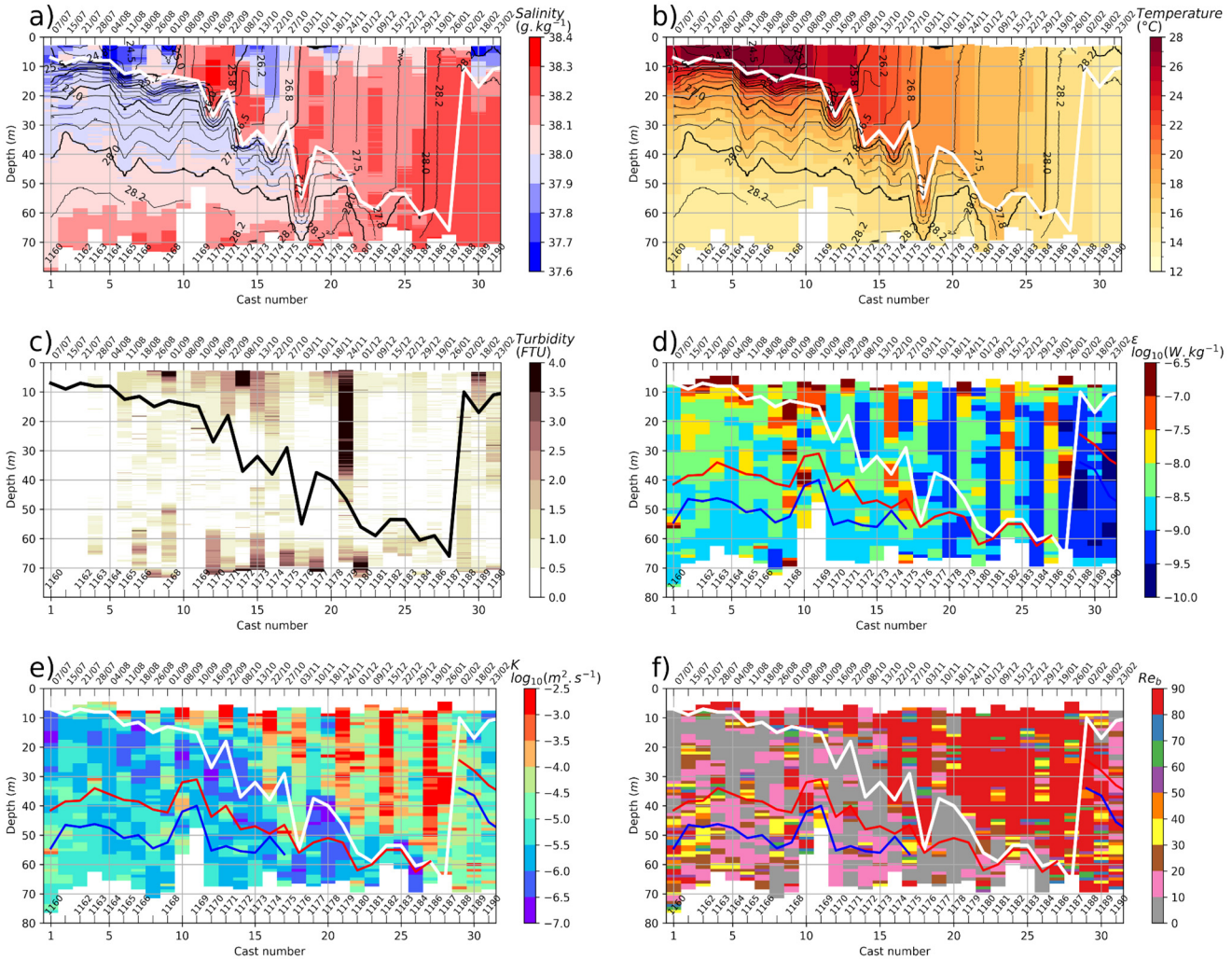

Figure 2. Temporal sequences of the vertical profiles of (**a**) salinity and density (black contours), (**b**) temperature and density (black contours), (**c**) turbidity, (**d**) dissipation rates of turbulent kinetic energy, (**e**) diffusion rates of turbulent kinetic energy, and (**f**) the buoyancy Reynolds number. MC casts are indicated over the cast number. Dates are shown on the upper x-axis. For all plots: main thick line indicates the *MLD*, red and blue lines indicate the average depth of the 1st and 2nd baroclinic modes, respectively.

3.1.1. Mixed Layer Depth

MLD is indicated on all plots by the thick line and shows a clear seasonal cycle: a stratified period in July–August, followed by a progressive deepening of the *MLD* from September to November, finally reaching a period when the water column is close to being fully mixed from December to January, followed by a surface re-stratification in February induced by a low salinity anomaly. This behavior in density is clearly driven by the freshwater contribution to the salinity at the surface and subsurface. A visual inspection of the *MLD* was finally performed. The *MLD* estimates were further checked, with a computed quality index Qc [74], following the detailed procedure given in [75]. The majority of *MLD* estimates were acceptable, with a Qc in the range [0.5–1.0] (not shown). Four of the *MLD* estimates presented a Qc < 0.5. For one cast (cast n°23), Qc could not be computed as the *MLD* was close to the seafloor; the *MLD* was set to the seafloor depth. Other casts with Qc < 0.5 (casts n°28, 29, 30) corresponded to the re-stratification period in February when the vertical structure of the profiles appears to mislead the *MLD* calculation. For those cases, a visual inspection confirmed that these estimates were acceptable.

3.1.2. Salinity and Turbidity

Relatively fresh waters persist all along the summer until early November, from the surface down to 50–60 m depth, after which they are rapidly replaced by salty waters that remain till the end of the record (Figure 2a). A salty bottom layer of 38.1 to 38.3 g kg^{-1} is visible below the 28.3 kg m^{-3} isopycnal layer all along the record. This seasonal salinity variability is associated with some patterns visible in the turbidity measurements (Figure 2c). A turbid bottom layer was co-located with the deep salty layer. Some turbid bottom patches are visible in September (e.g., cast n°12), and when the mixed layer is close to the bottom, from the end of October to December (e.g., cast n°17 or 22). This provides evidence of the re-suspension of sediments in a weakly tidal area and suggests that energetic processes are located between the *MLD* and the bottom boundary layer. Once a full vertical homogenization is achieved in January (the core of winter period), no additional turbid layers are observed. Looking at the subsurface, local turbid patches are present inside the mixed layer from September to November, with structures occupying a large part of the water column (cast n°21) and are present at the surface during the re-stratification period in February (cast n°30).

3.1.3. Turbulent Kinetic Energy Dissipation Rate ε

The seasonal sequence of vertical profiles of dissipation rates of turbulent kinetic energy shows maximum values between 10^{-7} and 10^{-6} W kg^{-1} (Figure 2d), distributed through patches in various parts of the water column. The summer period shows peak values above 10^{-8} W kg^{-1} in the *MLD* (cast n°6, 11, 13, 16, 18). Some patches from 10^{-8} and 10^{-7} W kg^{-1} are visible between the *MLD* and the mean depth of the 1st baroclinic mode (red line), following their depth variation between July and October. More intense patches are visible intermittently and locally on certain casts, with values between $5 \cdot 10^{-8}$ and 10^{-7} W kg^{-1} (e.g., cast n°9, 16, 17). Deep layers are associated with dissipation rates under $5 \cdot 10^{-9}$ W kg^{-1} that are generally located below the main depth of the 2nd baroclinic mode, even some intermittent intense structures can be observed (e.g., cast n°1, 6, 11). Note that minimum values close to $5 \cdot 10^{-10}$ W kg^{-1} are observed (the noise limit of the instrument is 10^{-11} W kg^{-1}). In winter, the dissipation rates are clearly intermittent: low ($5 \cdot 10^{-10}$ W kg^{-1}) throughout most of the water column (cast n°20, 23, 26, 28, 29, 31), or more intense (10^{-9} to 10^{-8} W kg^{-1}) on large fraction (cast n°21, 24, 27) with local peaks ($\varepsilon > 10^{-8}$ W kg^{-1} between 15 and 30 m at cast n°24, or 20 m at cast n°27).

3.1.4. Turbulent Eddy Diffusivity

The eddy diffusivity K was estimated using the Osborn relation [76] as $K_\rho = \Gamma\varepsilon \,/\, N^2$ (m^2 s^{-1}) with a mixing efficiency coefficient $\Gamma = 0.2$. A remarkably low diffusive layer ($K < 5 \cdot 10^{-6}$ m^2 s^{-1}) is visible during the destratification, occupying a 10 to 30 m thick layer below the *MLD* (Figure 2e). In July, some intensified patches can be observed from 30 to 70 m (cast n°1–4) in the depth ranges associated with the two first baroclinic modes. In the surface layers, the most intense values are between $5 \cdot 10^{-4}$ and $5 \cdot 10^{-3}$ m^2 s^{-1} (cast n°11, 13, 18, 24, 27) and, generally, large patches with values between $5 \cdot 10^{-5}$ and $5 \cdot 10^{-4}$ m^2 s^{-1} are observed (cast n°20, 23, 28) and few profiles show relatively low values ($K < 10^{-5}$ m^2 s^{-1}, cast n°19, 26, 31). The turbulent activity is quantified by the buoyancy Reynolds Re_b (see Section 2, Methods). For the GoN, the buoyancy Reynolds number (Figure 2f) shows that the stratified layers belong to the buoyancy-controlled regimes ($Re_b < 10$), except for intermittent cases ($10 < Re_b < 30$) around the main baroclinic depths, while the surface intermittent turbulence belongs to both buoyancy-controlled ($Re_b < 10$) and transitional regimes ($Re_b > 20$).

3.2. The Forcing Context of the Wind Stress, Buoyancy Fluxes, and Sea Waves during the Seasonal Survey

The time evolutions of the buoyancy fluxes, the surface wind stress, and the wave height are examined to build a simple scaling of the *MLD*.

3.2.1. Wind, Wave, and Heat Fluxes: A Seasonal Overview

In general, negative buoyancy fluxes strengthen the stratification of the water column while positive buoyancy fluxes weaken the stratification and may lead to surface convection and a deepening of the MLD. During summer and till mid-September, the daily averaged B_0 was always negative apart from three short episodes of positively buoyant days (Figure 3). In contrast, after mid-September, B_0 remained positive (or close to zero). Consequently, from the beginning of the observed period, the cumulative buoyancy flux decreased and reached a minimum level around mid-September (not shown) and then constantly increased from mid-October to reach a maximum at the end of the record. Buoyancy fluxes and the wind stress contribute both to mix the surface layer and deepening the MLD. A negative flux counteracts the wind stress by stabilizing the water column, while a positive flux will add its effect to the wind mixing by destabilizing the layers. The wind stress (Figure 3a) over the summer period is weak and shows few intermittent events before mid-September ($u_* < 5 \cdot 10^{-3}$ m s^{-1}). In September, relatively strong wind events started (u_* close to $8 \cdot 10^{-3}$ m s^{-1}), followed by three events during October (u_* close to 10^{-2} m s^{-1}). The three most energetic storms ($u_* > 10^{-2}$ m s^{-1}) occurred around the 20th of November, in January, and in February. The precipitation rates show intermittent events with values close to or larger than 20 mm d^{-1}, with a maximum of about 75 mm d^{-1} in early October, followed by intermittent rainy events during the rest of the period (Figure 3b). This time series is highly coherent with the river discharge (in blue). Wave heights are generally well correlated with the wind stress and reproduce the quiet and intensified periods (Figure 3c). Strong events show values of $H_S > 1$ m (e.g., mid-October) with peaks between 2 and 4 m (e.g., mid-November, or January and February). The associated Langmuir number (pink line) indicates critical periods with values of $La < 0.5$, a regime for which Langmuir cells should contribute to the mechanical mixing at the same time as the wind. Interestingly, we see a repeating regime from July to September, with values $La < 0.5$, that is probably due to the daily cycle of the summer breeze [2].

3.2.2. Forcings during the 24 h before the Casts, and the Observed Profiles

We hypothesize that the hydrology we observed for each weekly cast was the result of the processes that occurred in the hours before. We present in Figure 4a the synthesis of the forcings that occurred in the previous 24 h before each cast. Episodes of strong winds happened hours before the cast, inducing a "calm sea bias" at the time of our measurements. Moreover, the cast hour (generally around 8:30 am, sometimes later, see Table 1) positioned the observations at the transition between nocturnal and diurnal heat fluxes. Consequently, at the moment of measurements, the convective fluxes were expected to be weakening since their nocturnal maximum. Furthermore, heat fluxes can already stabilize the water column in the early morning at such latitude.

We propose to model the MLD (see Section 2, Methods) as the sum, L_{EC}, of the buoyancy effects (through the determination of a convective depth) and the wind stress effect (through the determination of an Ekman layer depth). Given the lagged correlations obtained thereafter in the study (when establishing correlations between ε and the forcings, see Section 3.4), we calculated the mean of the Ekman layer depth L_E in a window of 18 h before the cast. Positive L_{EC} values (out of surface) are finally ceiled to zero and values deeper than the bottom of the water column are limited to 75 m. In general, the Ekman layer is in good agreement with the MLD when the water column is stratified, but fails to represent it when destratification occurs (Figure 4b,c). We calculate the correlation coefficient (cc) and the p-value (pv) of the linear regression with the observations. When adding the convective contribution, a very good agreement is obtained (green curve; $cc = 0.86$; $pv = 3.86 \cdot 10^{-10}$). In some cases the convective layer depth overestimates the MLD ($L_{EC} - MLD > 10$ m, casts n°10, 11, 13, 16, Figure 4c) and we can substitute L_{EC} values with L_E to obtain a composite, significantly correlated with the MLD (0.93, p-value $5.40 \cdot 10^{-15}$, red line in Figure 4c).

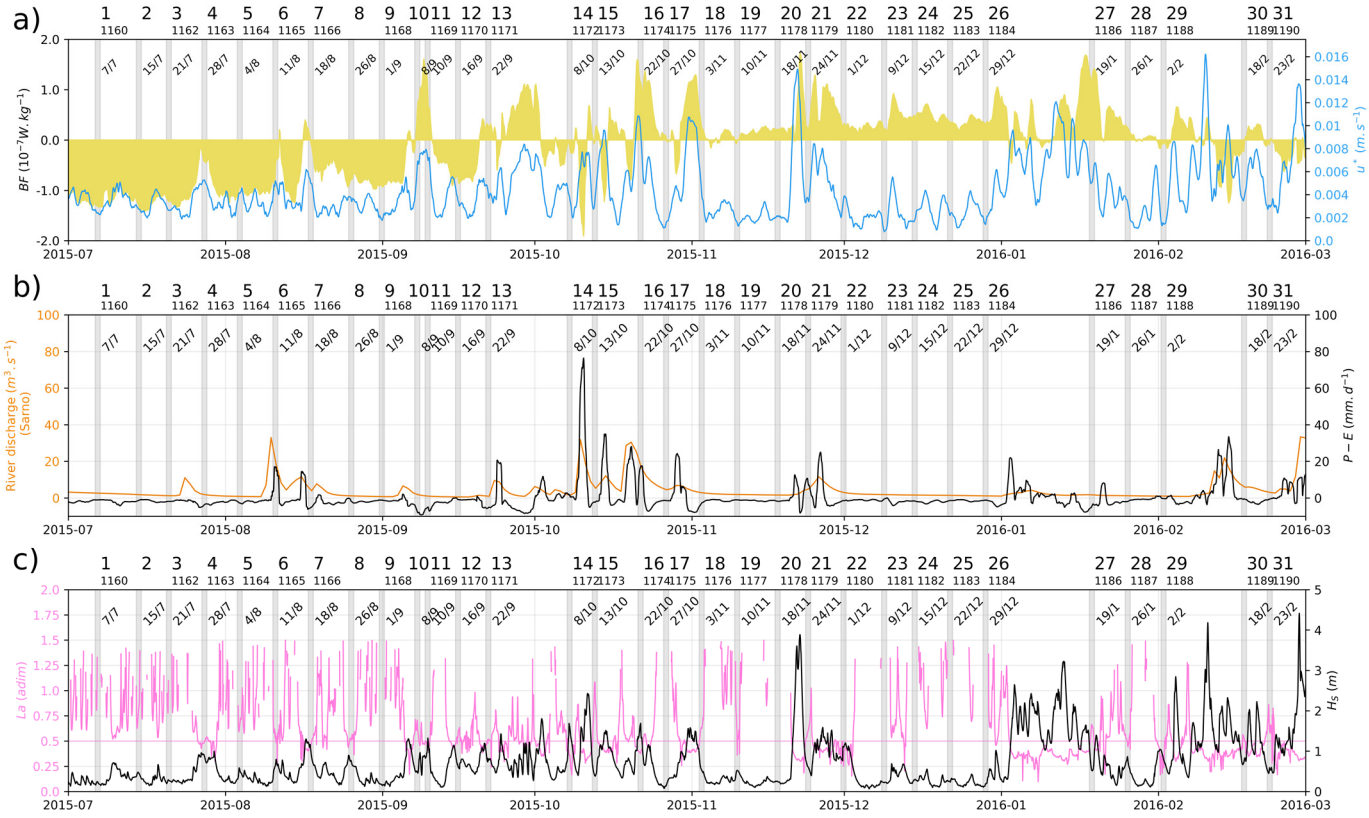

Figure 3. (**a**) Time series of the wind friction velocity (blue), buoyancy fluxes (plain yellow); (**b**) net precipitation rates (black) and river discharge (orange). River discharge is considered at the Sarno river's mouth (see Figure 1). (**c**) Time series of the significant wave height (black) and Langmuir number (pink). All plots: the time range of the 24 h preceding each cast is indicated with the gray backgrounds; cast's number (1–31) with the MC number (1160–1190, see Table 1) are indicated on top; cast's date is indicated below.

We show the observed hydrology at the moment of the cast (T, S, σ and MLD) in Figure 4d. Looking closer at the vertical structure, we can notice that the overestimations in the convection contribution coincide well with the presence of relatively freshwater parcels at the basis of the MLD, in the 5 m located below, independent of the surface or bottom salinity. Interestingly, when looking at the river's runoff, considering the cumulation of the discharges that occurred between the casts (Figure 4c, blue area; blue line in Figure 4d), we can identify consistently the two fresh episodes from the Sarno river that could have been advected westward (the river's mouth is located at the east) to the LTER-MC point. They coincide with casts n°6 and n°15 that are characterizing two distinct episodes of low surface salinity (37.6 and 37.8 g kg^{-1}, respectively). Once such freshwater is present in the coastal area, it opens the question of its persistence during the following days and weeks, as it is emphasized by the cases of "fresh MLD basis" (e.g., cast n°6, 10, 11, 13, 16, 17).

3.3. Observations of ε: Distributions into the Vertical Layers and at Single Depths

In this part, the time evolution of ε is characterized in the layers and periods that came out from the previous section. We use our results about the time course of some layers of interest (MLD, BC_1, BC_2) during the seasonal destratification to define vertical bins that describe the stratified layers: MLD–BC_1 as a transitional layer and BC_1–*bottom* as a bottom layer. At the same time, we characterize the seasonal variability in the surface layers by looking at two periods: July–October (JO, summer to autumn) and November–February (NF, autumn to winter). We complete, then, the overview by considering ε at single depths ($h = H/2$, MLD, $MLD/2$).

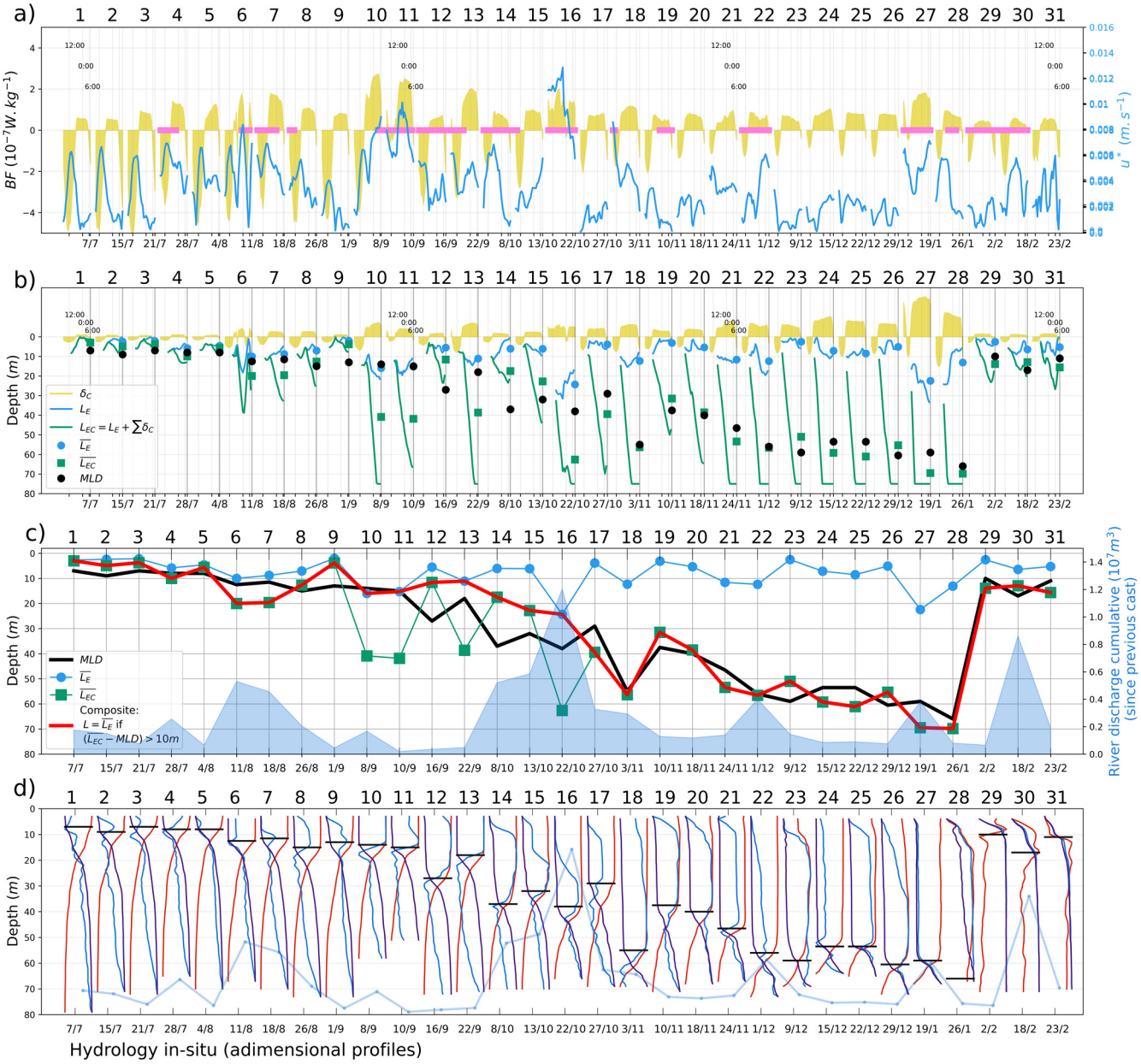

Figure 4. (**a**) Time series of wind stress (blue) and buoyancy fluxes (yellow) during the 24 h before each cast. Critical periods when $La < 0.5$ are indicated in pink. (**b**) Ekman layer L_E (blue), convective variation δ_C (yellow), and their combination L_{EC} (green) to compare to the observed MLD (black dots). Blue dots and green squares: L_E and L_{EC} averaged for 18 h before the cast. (**c**) Time course of the MLD (black), compared to L_E (blue) and L_{EC} (green). On the right y-axis, we show the cumulative of the Sarno's river discharge since the last cast. (**d**) Adimensionalized vertical profiles of T, S, σ (respectively, in red, blue, and dark purple). Black horizontal lines: MLD estimates; blue transparent in the background: cumulation of the Sarno's river discharge between the casts reproduced without units from (**c**).

3.3.1. Peaks

The time sequence of the profiles of dissipation rates exhibits a succession of peaks and minima, illustrating well the complexity of the vertical structure of the water column (Figure 5, left). When the water column is the most stratified (July to September), the surface local minimum of dissipation ($O(10^{-8})$ W kg^{-1}, located below the red area on the plot) is generally close to the observed MLD and may sign for a mixing surface layer. The

MLD deepens during the season and various local minima and maxima ε can be found between the surface and the MLD, showing a complex variability. Noteworthy, some can be observed repetitively below the MLD into layers close to the main baroclinic depths (e.g., in August, the peaks are around 40 m, repeated for three weeks). Some are close to the bottom, where they could sign for boundary effects. In the surface layers, other peaks can be observed when the water column is less stratified (e.g., in December, around 20 m and 30 m) and may be due to the intermittency of the surface forcings.

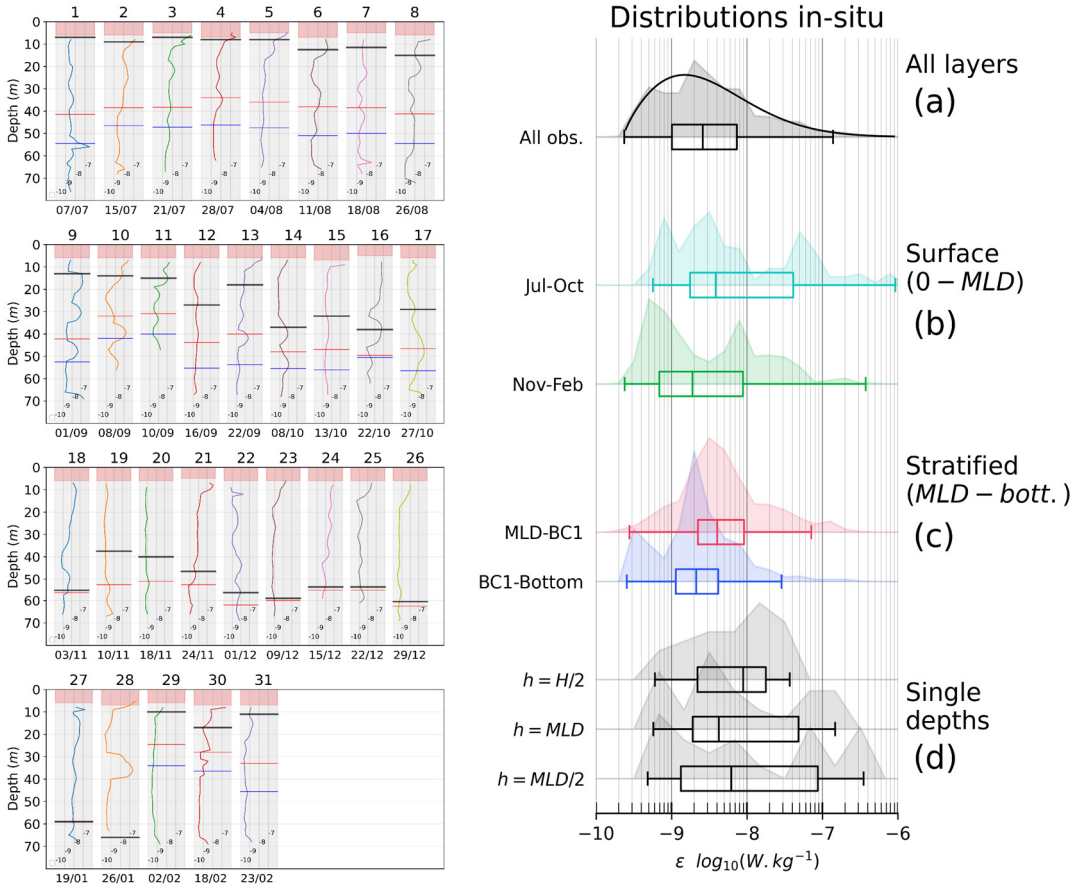

Figure 5. (**left**) Vertical profiles of $\varepsilon \left(\mathrm{W\ kg^{-1}}\right)$ *in log* 10, during the two periods July–October (JO), then November–February (NF). Red areas indicate the surface part that is removed from the statistics. Black lines: MLD. Red and blue lines: average depths of the two first baroclinic modes BC_1 and BC_2, respectively. (**a**–**c**) Boxplots of ε ((**a**): all values; (**b**): surface layers during the two periods JO and NF; (**c**): stratified layers, $MLD - BC_1$ and $BC_1 - bottom$). Shapes of the associated PDFs are plotted in color (black line on (**a**): Burr type XII fit). (**d**) Boxplots of epsilon at single depths ($h = H/2,\ MLD,\ MLD/2$).

3.3.2. Distributions

We characterize the statistical distribution grouping the observations by layers and periods. We show the general distribution in Figure 5a and the surface and stratified layers in Figure 5b,c. Finally, in Figure 5d, we show the distribution obtained when considering only single depths (not vertical bins). This will be used in the next section for the modelization of ε. In general, the probability density function (PDF) of epsilon (Figure 5a) is better described by the Burr type XII distribution than the log normal (not shown), as the distribution is not symmetrical and displays an important tail. Even with this good agreement, we note that the distribution seems to have a bi-modal component, with a first peak centered on $5.0 \cdot 10^{-10}$ W kg^{-1} and a second close to $2.0 \cdot 10^{-9}$ W kg^{-1}. The asymmetry is visible too when considering the subsurface layers (Figure 5b). The

two distributions show different peaks when examining the distributions by time period. With more details, JO (mean: $7.20 \cdot 10^{-9}$ W kg^{-1}, median: $3.85 \cdot 10^{-9}$ W kg^{-1}) is shifted toward higher dissipations with an additional peak close to $5.0 \cdot 10^{-8}$ W kg^{-1}, while NF is weaker and without such a peak (mean: $2.90 \cdot 10^{-9}$ W kg^{-1}, median: $1.90 \cdot 10^{-9}$ W kg^{-1}). In the stratified layers (Figure 5c), ε in the transition layers ($MLD - BC_1$, in red) displays a shape that is the closest to the log normality (from a classification test using the sum of the square errors between the data and the fitted distribution) with a mean value centered on $4.81 \cdot 10^{-9}$ W kg^{-1}. Differently, the deepest layer ($BC_1 - bottom$, in blue) is shifted toward lower dissipations (mean: $2.21 \cdot 10^{-9}$ W kg^{-1}) and displays the same bi-modal component as the upper layers (Figure 5a).

3.3.3. Single Depths

We show in Figure 5d the boxplots obtained at single locations ($h = H/2,\ MLD,\ MLD/2$) that are different from the more complete distributions. We want to see if general properties from the layer approach (e.g., vertical bins) can be reproduced by considering only single depths. The distribution of the layer $h = H/2$ describes the middle of the water column and contains ε occurrences characterizing both surface and stratified layers. Distributions at $h = MLD,\ MLD/2$ are comparable and closely reproduce the main peaks seen in the subsurface distributions in Figure 5b. These single depths catch the variability observed in the layers.

3.4. A Model for ε in the Subsurface Layer

Time series of forcings are used here to infer more finely the role of each contributor to the observed dissipation, parameterized using the bulk parameters (B_0, u_*, L_a) following the model of [62] (and named thereafter B12). Dissipation rates are given by the linear combination of the effect of wind, wave, and convection at the depth h, as $\varepsilon_{B12} = \varepsilon_{wind} + \varepsilon_{wind-wave} + \varepsilon_{conv} = E_S u_*^3/h + E_L w_{*L}^3/h + E_C w_*^3/h$ (see Section 2, Methods). Each contributor is quantified during the 24 h preceding the observations of ε (Figure 6) and summed to compare the model to the observed dissipation rates (Figure 7). Finally, we exploit the seasonal coverage of the survey to produce a monthly cycle of ε.

3.4.1. Moments of the Measurements

Calm sea bias. In general, the casts were gathered when the weather conditions allowed outings to the sea as well as a safe deployment of the various instruments. The data presented in this study include a calm sea bias that is well illustrated here. We see in Figure 6 that casts are generally performed after possible intense atmospheric events implying strong winds or large waves.

Timing. In Results 3.2 we obtained a good agreement between the MLD and the vertical scales associated with the forcings evaluated during the 18 h preceding the cast. Coherently, this time scale seems to apply to ε too: we can observe that 18 h before the casts, values of ε_{wind} (blue) or $\varepsilon_{wind-wave}$ (pink) are, generally, of the same order as the observations (e.g., casts n°7, 19, 20, 27). The term ε_{conv} (yellow) is of the same order as the two others in summer, then, progressively increases with the seasonal setting of stronger unstable buoyancy fluxes.

Sunrise bias. Looking closer at the timing of ε_{conv}, we see that our observations include a *sunrise bias*. Measurements were conducted between 8:00 and 10:00, which corresponds to the ascending phase of the daily heat fluxes. The diurnal cycle sets, the buoyancy fluxes progressively switch to stabilize the water column, and ε_{conv} is not evaluated ($B_0 > 0$). Moreover, nocturnal values are generally high (between 10^{-7}–10^{-8} W kg^{-1}) and tend to decrease to 10^{-9} W kg^{-1} within one hour after the sun rises. Given such a timing, the 1 h temporal resolution of the ERA5 dataset could lead to a model misevaluation: a possible source of overestimation due to strong nocturnal values or underestimation due to not evaluating the model under stable fluxes.

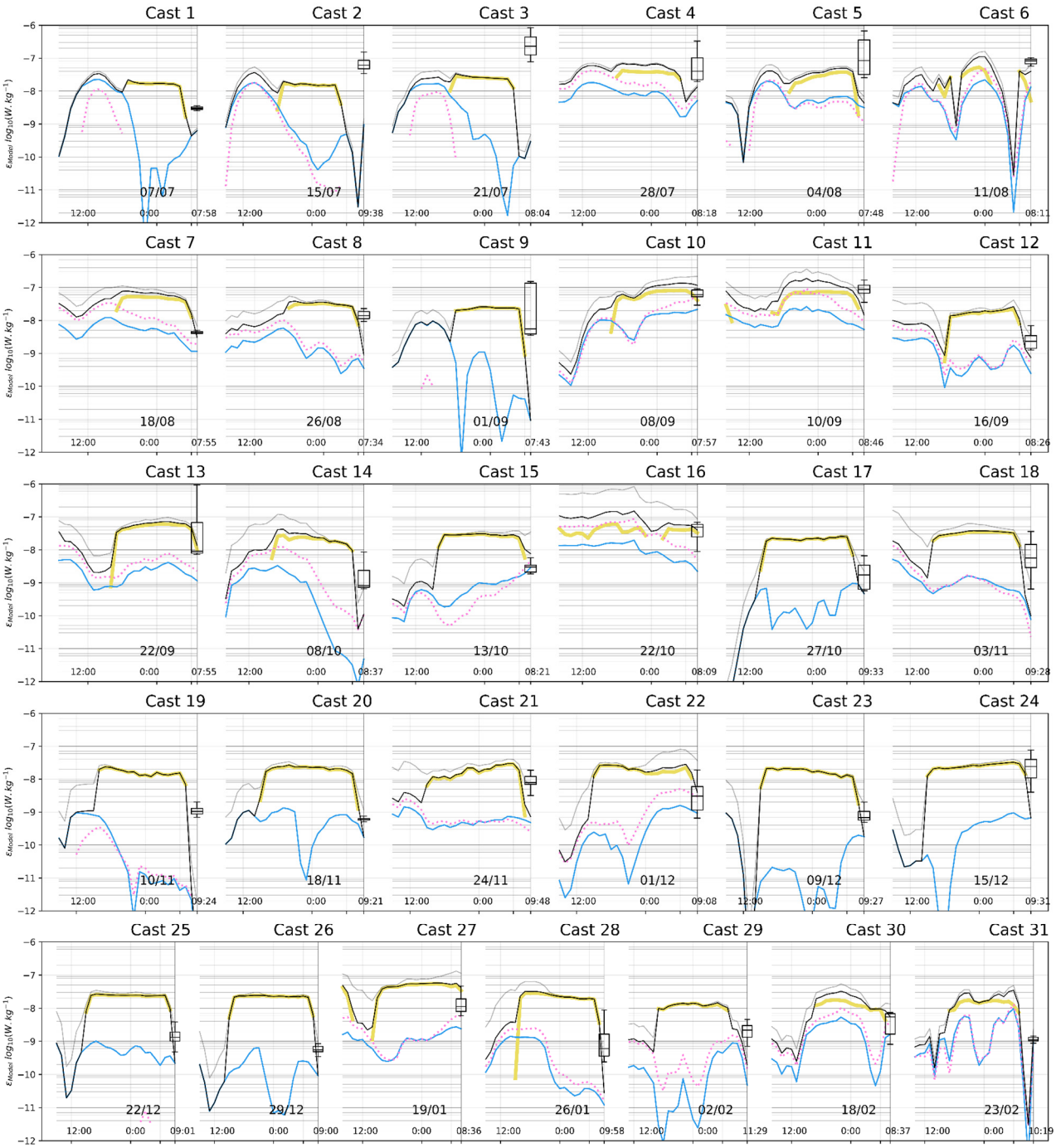

Figure 6. Time series of ε_{B12}. Total of the dissipation rates (black) and its decomposition through the contributions of the wind stress (blue), the buoyancy fluxes (yellow), the wind–wave Langmuir regime (pink). Here, we show 24 h before each cast. Model is evaluated at $h = MLD$ (and at $h = z_{surface}$ to provide an upper limit, shown in gray). Boxplots of ε in situ (bin: $surface - MLD$, excluding the first meters) are shown on the vertical line indicating the moment of the cast.

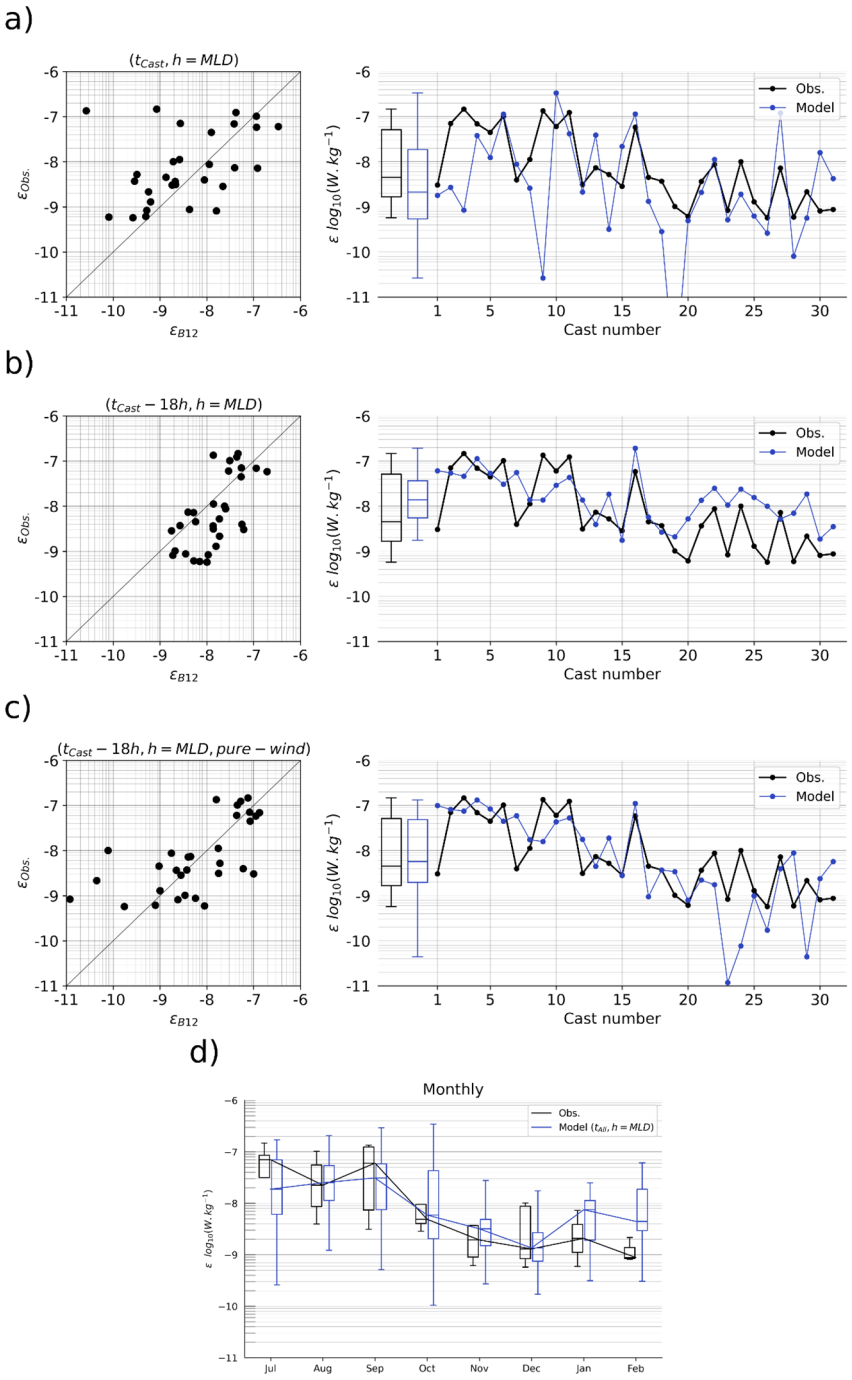

Figure 7. Comparisons between observations and models. (**Left**) Scatterplots (ε_{Obs},ε_{Model}); (**right**) boxplots and sequences of values (black: observation; blue: model). To confront the observations, ε_{Model} is evaluated at $h = MLD$, at $t = t_{Cast}$ (**a**), $t = t_{Cast} - 18$ h (**b**), and $t = t_{Cast} - 18$ h using only the wind term (**c**). For each ε_{Model} distribution, a mean factor has been applied: $mf = 2.88$ on (**a**), $mf = 1.91$ on (**b**) and $mf = 1.55$ on (**c**). (**d**) Monthly distributions of ε. To estimate the model, all the days of the survey (July 2015–February 2016) are considered (i.e., not only calm sea moments). Model is corrected with $mf = 2.88$.

3.4.2. Model vs. Observations

General performance. To assess the performance of the model, we calculate the correlation coefficient (cc) and the p-value (pv) of the linear regression with the observations and the mean factor $mf = \varepsilon_{Obs}/\varepsilon_{Model}$. The best agreement is obtained when evaluating

the model at $h = MLD$ ($cc = 0.43$; $pv = 0.0154$; $mf = 2.88$), which is closely comparable to using $h = MLD/2$ ($cc = 0.46$; $pv = 0.0267$; $mf = 4.84$). The distributions are presented in Figure 7a (left: scatterplots; right: boxplots and sequence of values).

18 h before. Additionally, we estimated ε_{Model} every hour and tested its correlations with ε_{Obs} using temporal lags of 1 h in the past. A preliminarily check of the autocorrelations of u_*, H_S, and B_0 times series indicated a temporal window properly decorrelated after 13 h in the past for u_*, and after 16 h for H_S (windows for B_0 were between 4–8 h, around 13 h, and after 18 h). Taking this into account, we calculated the correlations between ε_{Obs} and $\varepsilon_{Model}(h = MLD, t = t_{Cast} - 18\text{ h})$ and we obtained a good agreement (Figure 7b; $cc = 0.65$; $pv = 7.42 \cdot 10^{-5}$; $mf = 1.91$). Relative to the casts, this lag of 18 h corresponds to considering the forcings between 14:00 and 16:00 the day before. This hour range is generally associated with low or non-contributing buoyancy fluxes compared to the morning phase. Consequently, with this lag we can expect that the model represents mainly the effect of wind. When considering the case of a pure-wind estimation (i.e., $\varepsilon_{B12} = 2\,u_*^3/h$, Figure 7c), correlations are still significative ($cc = 0.63$; $pv = 1.27 \cdot 10^{-4}$; $mf = 1.55$). We hypothesize that the dissipation observed 18 h later in our casts could be partially due to the inertial adjustment of the shears generated by the wind at the basis of the *MLD*. The instruments used on board did not include an ADCP (acoustic doppler current profiler) and we did not have measurements of the speed of ocean currents in the water column at the time the vertical profiles were performed. We do not have information to know the state of the velocity field, its vertical and horizontal gradients, and the energetics associated with them. This particularly limits the development of our study and its conclusions.

Seasonal cycle. We fruitfully exploit the sequence of the weekly snapshots from our observations to establish a seasonal cycle for ε based on the monthly time scale. From the summer 2015 to the winter 2016, we characterize a half-seasonal cycle (Figure 7d). In July, the model underestimated the observations, whose higher median value indicates that observations included more energetic processes not reproduced by the model. August and September indicate ranges of variability comparable to the model. A wide variability was obtained in October, while the observations were clearly more limited, maybe due to the conditions at sea that prevented sampling in bad weather conditions. Variability in November seems comparable. More intense events are captured by the observations in December. January and February indicate wide ranges that were partially covered by the observations.

The calm sea bias we have in our data is illustrated too in Figure 7d. When considering all the days between July 2015 and February 2016, we include de facto the energetic events when the conditions at sea were not compatible for a safe deployment and sampling. Compared to the model in this period between 8:00 and 12:00, the median value of the observations is weaker (observations centered on $3.0 \cdot 10^{-9}$ W kg^{-1}; model on $1.0 \cdot 10^{-8}$ W kg^{-1}) and a more limited dispersion. We show that we missed a large part of the variability range and, consequently, the most intense values of dissipation.

4. Discussion

4.1. A Coastal Station at the Crossroad between Offshore and Riverine Systems?

Our observations showed that the nearby Tyrrhenian Sea acts as a source of salty water, which was observed at depth from July to October and throughout the water column later in the year. This causes the subsurface layers to be susceptible to weak salt fingering regimes [77]. The lateral salinity gradient has yet to be determined, but it is probably an important factor to consider when estimating the mixed layer depth (*MLD*). Using relatively low-density thresholds for the *MLD* calculation can lead to underestimation due to the contribution of salinity. However, we found a good agreement between the *MLD* calculated using temperature (0.2 °C) and the *MLD* calculated using a strong density threshold (0.15 kg m^{-3}). If $MLD_\theta^{0.2°C}$ was deeper than $MLD_\sigma^{0.15\text{ kg m}^{-3}}$, we retained its value. We also observed the influence of freshwater in the system. The nearby Sarno River, located in the northeast corner of the GoN, is a potential source of freshwater anomalies that

can propagate along the east side of the Gulf. This river could be the main source of the low salinity surface waters observed between July and October (as well as the re-stratification in February). The study [1] noticed that this influence was mostly confined to the eastern part of the GoN and our study suggests its freshwater parcels may reach the LTER-MC site too. In addition, local trapping of freshwater at the coast due to daily oscillations of breeze winds (as described in [2]) may contribute to a pooling effect during the summer months.

4.2. What Is the Effect of Wind and Buoyancy Forcings on Setting the MLD?

Our results suggest that subsurface layers associated with relatively fresh water can inhibit the penetration of surface forcings into the water column. We developed an *MLD* model that combines the contributions of wind and convection. Forcings were considered within an 18 h window before each cast and the model provided a good agreement with the observations. Our results are consistent with [68], which found a better agreement between the *MLD* and the Ekman layer when the wind stress was considered 10–12 h beforehand. We obtained the best results using an 18 h window. We also included the impact of hourly buoyancy fluxes on the *MLD*. The good agreement with the observations suggests that wind and buoyancy forcings are the main drivers of mixing in this area. However, we identified overestimations due to convective terms when relatively low salinity layers were present below the *MLD*, which is not accounted for in the model. This suggests that the presence of such low salinity layers may inhibit convective penetration and contribute to the *MLD*. These layers often coincide with periods of intense runoffs, highlighting the connectivity between the LTER-MC station and freshwater sources along the coastline. The presence of turbidity patches in the subsurface layers, particularly during winter, may also be indicative of runoff discharging sediments at various coastal points after rainfalls (as described in [78]). The role of the wind in advecting these nutrient-rich waters, potentially influenced by mesoscale and sub-mesoscale features in the area (as described in [79]), remains to be explored.

4.3. How Turbulent Is the Coastal Environment?

By determining the *MLD* and timing and contributions of forcings, we were able to analyze the observations of ε in the surface and stratified layers (e.g., the average depths of the main baroclinic mode; the bottom layer) and periods (summer to autumn with moderate winds and buoyancy fluxes, and autumn to winter with stronger events). This allowed us to statistically characterize ε, as recently studied in the open ocean [80,81]. Our results showed that the dissipation rates in the mixed layer are more similar to a Burr XII distribution than a lognormal distribution. This warrants further investigation, as a lognormal behavior is typically expected for intermittent features such as these [38]. In general, our distributions show moderate values (10^{-9}–10^{-8} W kg^{-1}) with few energetic occurrences (above 10^{-7} W kg^{-1}), indicating a relatively quiescent environment rather than fully isotropic turbulence. This may be due to the use of a small research vessel that did not allow for sampling in rough weather, leading to an underestimation of temporal intermittency. Additionally, observations were always performed in the morning, when buoyancy fluxes stabilize the water column, which may also contribute to the calm sea bias.

4.4. Is the Ocean Surface Boundary Layer (OSBL) Influenced by Coastal Boundaries?

The coastal environment may be less energetic than offshore conditions in the GoN, but the presence of both vertical (bottom layer) and horizontal (coastline) boundaries likely complicates the local motions and circulations, which may respond non-linearly to various forcings [82,83]. Evidence of sediment resuspension in a weakly tidal area, indicated by the presence of a turbid bottom layer with near-bottom peaks, suggests energetic processes between the *MLD* and the bottom boundary layer. This has been observed in shallow bays with distinct nepheloid layers produced by internal bores leading to breaking internal waves [84,85]. Processes such as resuspension due to bed shear stress caused by wind, waves, and currents (as described in [86]) need to be further investigated. Our observations

of ε in the water column show a rich collection of peaks that are difficult to systematically link with other variables such as turbidity and chlorophyll. As a result, it is difficult to determine a single mixing depth as established in recent studies [75,87]. The vertical variability of ε observations prevented us from identifying a unique depth, as it exhibits many minima and maxima. This raises questions about the validity of the OSBL concept in coastal areas due to the proximity to the bottom. We identified the transitional layer thickness from the low buoyancy Reynolds number below the *MLD*, where vertical motions are suppressed by strong buoyancy (as described in [54]). During the seasonal cycle, this layer progressively mixes with the rest of the water column and eventually with the bottom layer. Instead of the typical four-layer structure (surface, transition, thermocline, bottom), the vertical structure in this area is more like a three-layer system (surface, transition, bottom) with stratified layers that mix during seasonal destratification, eventually forming a single mixed layer reaching the bottom in winter.

4.5. Which Processes Could We Miss?

Observations of ocean currents, fronts, and internal waves are lacking in our study, preventing us from understanding the velocity field, its bulk and fine-scale shears, and the horizontal fronts in more detail. Nevertheless, we can list here various processes of interest that could be investigated in the next studies with the help of current meters in surface and through the water column.

In such coastal areas, freshwater runoffs are expected to be of importance in straining the density fields, by stabilizing the water column and suppressing small-scale mixing [9]. In their recent work, ref. [88] identified two types of vertical structures prevailing in zones influenced by a river's plume, very similar to the density profiles we observed during our survey. Moreover, in weakly tidal locations, the straining caused by the ebb tide is expected to be weaker and should be driven instead by the direct freshwater input from rivers, with a major role being given to the onshore or offshore wind that can retain or spread the fresh coastal flow [10].

In the absence of data, the influence of lateral density gradients was not considered in our study. It would be of importance in future studies to estimate the horizontal buoyancy gradient and the horizontal velocity field in order to quantify the relative importance of the lateral buoyancy flux (driven by wind or eddies) and the surface buoyancy flux due to heat transfer [89]. In this perspective, the role of wind and the precise tracking and quantification of fresh parcels should be investigated.

Internal waves may be a source of mixing, also supported by motions in Langmuir cells forced by the surface wave field [11,90]. The role of Langmuir cells in the wind–wave coupling needs further investigation in the Gulf of Naples, as the authors report observations in the surface near the coast under constant wind conditions (white streaks of nearly 300 m long, with clumps of floating algae).

Our results suggest the importance of the inertial response in the stratified layers. The vertical microscale shear events observed in the stratified layers of the water column may be caused by wind-driven inertial oscillations in the mixed layer, responding to the wind forcing that occurred 18 h before [68]. Recently, ref. [91] highlighted the role of coastal reflection in generating such wind-driven inertial oscillations, propagating offshore and intensifying the shear in the region below the mixed layer. In shallow waters, the presence of a bulk shear between the main flow and the bottom drag, combined with phase shifts due to surface wind stress between upper and lower layers of the water column, may enhance shear and lower the Richardson number, leading to instability through the shear spike mechanism [92,93]. This process may be amplified in coastal areas influenced by freshwater inputs due to the straining of the stratification caused by runoffs [10].

Bathymetry may also play a role in the GoN. Internal waves generated by current–topography interactions can radiate from the shelf toward the coast and affect the first two baroclinic modes [94]. The steep canyons in the GoN, particularly the Dohrn Canyon, may serve as a source for onshore propagating waves. The various bathymetric features

near the coast, such as the Banco della Montagna, the Ammontatura channel, and the Mt. Somma–Vesuvius complex ([95], their Figure 1), may also contribute to current–topography interactions. In addition, the presence of Kelvin coastal trapped waves in the area has been proposed by [96].

4.6. Long-Term Time Series Completed by Weekly Snapshots of Microstructure Observations: Can We Improve the Coastal Modeling?

Our microstructure survey was part of the long-term monitoring of the coastal area of the Gulf of Naples by the Marechiara project which started in 1984 and has run until now. It provided a useful time series, from July 2015 to February 2016, with valuable insights about the seasonal cycle of stratification and dissipation in the GoN. These observations can be used to validate and improve models of the region. The general agreement with the model by Belcher et al. 2012 [62] encourages us to estimate the dissipation rates in the *MLD* from bulk parameters, available at the regional scale in a recent public re-analyzed dataset (ERA5, Copernicus [57]). These estimates can then be applied to longer time series to understand the inter-annual variability of the mixing in the GoN, and to relate it to the rich biological observations already available. Long-term observations of coastal areas such as the GoN are crucial for understanding the various processes at work and which ones may be the most sensitive to future climate change. Our study highlights the need for microstructure observations that cover a wide range of space and time scales [38]. Meeting these challenges in the future [39] will require the deployment of microstructure devices on moorings and wirewalker systems [97,98] or dedicated drifters like Argo floats [99]. The mechanisms driving convection, shear, and mixing at fine scales, which ultimately lead to the mixed layer deepening, can be significantly affected by long-term changes in heat, freshwater, and wind [100]. In conclusion, the GoN, as a shelf region with weak tides, is a suitable location to study processes less energetic than tides, such as internal waves or even double diffusion, in addition to the impact of global warming and increased stratification [3,101].

5. Conclusions

The measurement campaign in the Gulf of Naples (GoN) between July 2015 and February 2016 showed the seasonal deepening of the mixed layer, which was associated with intermittent dissipation rates of turbulent kinetic energy (from 10^{-9} to 10^{-7} W kg^{-1}). Wind stress, buoyancy fluxes, and waves were identified as the main forcings influencing the shallow waters of the GoN. Turbulence in the coastal environment is generally moderate, but the use of a small research vessel and the limited temporal coverage may have underestimated its intermittency. The GoN is also influenced by freshwater inputs, such as runoffs from the Sarno River and local pooling effects. The presence of low salinity layers below the mixed layer depth can inhibit convective mixing and contribute to setting the mixed layer depth. In terms of vertical structure, the water column at the LTER-MC point in the GoN may be better described as a three-layer system, rather than the typical four-layer system, with the stratified layers overlapping and forming a single mixed layer in winter. Future microstructure observations of ocean currents, fronts, internal waves, and Langmuir cells, as well as the stratification response to storms and the role of wind in advecting nutrient-rich waters, will improve our understanding of the processes at work in the GoN.

Author Contributions: Conceptualization, F.K., F.C., D.I., B.F. and P.B.-A.; methodology, F.K., B.F. and P.B.-A.; software, F.K. and B.F.; validation, F.K. and B.F.; formal analysis, F.K., D.I., B.F. and P.B.-A.; investigation, F.K.; resources, F.C. and D.I.; data curation, F.C. and F.K.; writing—original draft preparation, F.K., B.F., P.B.-A. and D.I.; writing—review and editing, F.K., B.F., P.B.-A. and D.I.; visualization, F.K.; supervision, D.I. and F.C.; project administration, F.C. and D.I.; funding acquisition, F.C. and D.I. All authors have read and agreed to the published version of the manuscript.

Funding: This research was funded by the Stazione Zoologica Anton Dohrn. The research program LTER-MC is supported by the Stazione Zoologica Anton Dohrn.

Data Availability Statement: The ocean in-situ microstructure data that support the findings of this study are available online under netcdf format on https://zenodo.org/record/4306862#.X8qt8bIReHo, accessed on 6 July 2022, (DOI: 10.5281/zenodo.4306861), or from the corresponding author, F.K., upon request. The external data that support this study are openly available: ERA5 ECMWF reanalysis for the global climate and weather (https://doi.org/10.24381/cds.adbb2d47, accessed on 6 July 2022); the River discharge and related historical data from the European Flood Awareness System (https://doi.org/10.24381/cds.e3458969, accessed on 6 July 2022). A preliminary version of this study is still available as a pre-print on the Earth and Space Science Open Archive https://www.essoar.org/doi/10.1002/essoar.10505074.3, accessed on 6 July 2022.

Acknowledgments: We would like to thank all the LTER-MC team. Special thanks must be given to the commandants and crews of the R/V Vettoria. And we are grateful to Justine Mc Millan from Rockland Scientific International, thanks to her for all the support, help, and insights she provided to help release this study.

Conflicts of Interest: The authors declare no conflict of interest.

References

1. Cianelli, D.; Uttieri, M.; Buonocore, B.; Falco, P.; Zambardino, G.; Zambianchi, E. Dynamics of a Very Special Mediterranean Coastal Area: The Gulf of Naple. In *Mediterranean Ecosystems: Dynamics, Management and Conservation*; Williams, G., Ed.; Nova Science Publishers: New York, NY, USA, 2012; Chapter 7; pp. 129–150.
2. Cianelli, D.; D'Alelio, D.; Uttieri, M.; Sarno, D.; Zingone, A.; Zambianchi, E.; Ribera d'Alcala, M. Disentangling Physical and Biological Drivers of Phytoplankton Dynamics in a Coastal System. *Sci. Rep.* **2017**, *7*, 15868. [CrossRef]
3. Woodson, C. The Fate and Impact of Internal Waves in Nearshore Ecosystems. *Annu. Rev. Mar. Sci.* **2018**, *10*, 421–441. [CrossRef]
4. Volosciuk, C.; Maraun, D.; Semenov, V.A.; Tilinina, N.; Gulev, S.K.; Latif, M. Rising Mediterranean Sea Surface Temperatures Amplify Extreme Summer Precipitation in Central Europe. *Sci. Rep.* **2016**, *6*, 32450. [CrossRef] [PubMed]
5. Koseki, S.; Mooney, P.A.; Cabos, W.; Gaertner, M.Á.; de la Vara, A.; Aleman, J.J.G. Modelling a Tropical-like Cyclone in the Mediterranean Sea under Present and Warmer Climate. *Nat. Hazards Earth Syst. Sci.* **2020**, *21*, 53–71. [CrossRef]
6. Zhang, W.; Villarini, G.; Scoccimarro, E.; Napolitano, F. Examining the Precipitation Associated with Medicanes in the High-Resolution ERA-5 Reanalysis Data. *Int. J. Climatol.* **2021**, *41*, E126–E132. [CrossRef]
7. Kokoszka, F.; Le Roux, B.; Iudicone, D.; Conversano, F.; Ribera d'Alcalà, M. Long-Term Variability of the Coastal Ocean Stratification in the Gulf of Naples: Two Decades of Monitoring the Marine Ecosystem at the LTER–MC Site, between Land and Open Mediterranean Sea. *Mar. Ecol.* **2022**. [CrossRef]
8. Compilation Group GEBCO. *GEBCO 2020 Grid*; British Oceanographic Data Centre, National Oceanography Centre, NERC, UK: Liverpool, UK, 2020. [CrossRef]
9. Liu, J.; Liang, J.-H.; McWilliams, J.; Sullivan, P.; Fan, Y.; Chen, Q. Effect of Planetary Rotation on Oceanic Surface Boundary Layer Turbulence. *J. Phys. Oceanogr.* **2018**, *48*, 2057–2080. [CrossRef]
10. Simpson, J.; Brown, J.; Matthews, J.; Allen, G. Tidal Straining, Density Currents, and Stirring in the Control of Estuarine Stratification. *Estuaries* **1990**, *13*, 125–132. [CrossRef]
11. Verspecht, F.; Rippeth, T.; Howarth, M.J.; Souza, A.; Simpson, J.; Burchard, H. Processes Impacting on Stratification in a Region of Freshwater Influence: Application to Liverpool Bay. *J. Geophys. Res.* **2009**, *114*. [CrossRef]
12. Lucas, N.; Grant, A.; Rippeth, T.; Polton, J.; Palmer, M.; Brannigan, L.; Belcher, S.E. Evolution of Oceanic near Surface Stratification in Response to an Autumn Storm. *J. Phys. Oceanogr.* **2019**, *49*, 2961–2978. [CrossRef]
13. Sullivan, P.; McWilliams, J. Langmuir Turbulence and Filament Frontogenesis in the Oceanic Surface Boundary Layer. *J. Fluid Mech.* **2019**, *879*, 512–553. [CrossRef]
14. Iermano, I.; Liguori, G.; Iudicone, D.; Buongiorno Nardelli, B.; Colella, S.; Zingone, A.; Saggiomo, V.; Ribera d'Alcalà, M. Filament Formation and Evolution in Buoyant Coastal Waters: Observation and Modelling. *Prog. Oceanogr.* **2012**, *106*, 118–137. [CrossRef]
15. Li, S.; Li, M.; Gerbi, G.; Song, J.-B. Roles of Breaking Waves and Langmuir Circulation in the Surface Boundary Layer of a Coastal Ocean. *J. Geophys. Res. Ocean.* **2013**, *118*, 5173–5187. [CrossRef]
16. Li, Q.; Fox-Kemper, B. Assessing the Effects of Langmuir Turbulence on the Entrainment Buoyancy Flux in the Ocean Surface Boundary Layer. *J. Phys. Oceanogr.* **2017**, *47*, 2863–2886. [CrossRef]
17. Taylor, J. Accumulation and Subduction of Buoyant Material at Submesoscale Fronts. *J. Phys. Oceanogr.* **2018**, *48*, 1233–1241. [CrossRef]
18. Liang, J.-H.; Wan, X.; Rose, K.; Sullivan, P.; McWilliams, J. Horizontal Dispersion of Buoyant Materials in the Ocean Surface Boundary Layer. *J. Phys. Oceanogr.* **2018**, *48*, 2103–2125. [CrossRef]
19. Dingwall, J.; Chor, T.; Taylor, J. Large Eddy Simulations of the Accumulation of Buoyant Material in Oceanic Wind-Driven and Convective Turbulence. *J. Fluid Mech.* **2023**, *954*. [CrossRef]
20. McWilliams, J.; Huckle, E.; Liang, J.-H.; Sullivan, P. The Wavy Ekman Layer: Langmuir Circulations, Breaking Waves, and Reynolds Stress. *J. Phys. Oceanogr.* **2012**, *42*, 1793–1816. [CrossRef]

21. Gargett, A.; Grosch, C. Turbulence Process Domination under the Combined Forcings of Wind Stress, the Langmuir Vortex Force, and Surface Cooling. *J. Phys. Oceanogr.* **2014**, *44*, 44–67. [CrossRef]
22. Liu, J.; Liang, J.-H.; Xu, K.; Chen, Q.; Ozdemir, C. Modeling Sediment Flocculation in Langmuir Turbulence. *J. Geophys. Res. Ocean.* **2019**, *124*, 7883–7907. [CrossRef]
23. Tejada-Martínez, A.; Grosch, C. Langmuir Turbulence in Shallow Water. Part 2. Large-Eddy Simulation. *J. Fluid Mech.* **2007**, *576*, 63–108. [CrossRef]
24. Brody, S.; Lozier, M. Changes in Dominant Mixing Length Scales as a Driver of Subpolar Phytoplankton Bloom Initiation in the North Atlantic. *Geophys. Res. Lett.* **2014**, *41*, 3197–3203. [CrossRef]
25. Sverdrup, H. On Conditions for the Vernal Blooming of Phytoplankton. *ICES J. Mar. Sci.* **1953**, *18*, 287–295. [CrossRef]
26. Kiørboe, T.; Mackenzie, B. Turbulence-Enhanced Prey Encounter Rates in Larval Fish: Effects of Spatial Scale, Larval Behaviour and Size. *J. Plankton Res.* **1995**, *17*, 2319–2331. [CrossRef]
27. Prairie, J.; Sutherland, K.; Nickols, K.; Kaltenberg, A. Biophysical Interactions in the Plankton: A Cross-Scale Review. *Limnol. Oceanogr. Fluids Environ.* **2012**, *2*, 121–145. [CrossRef]
28. Barton, A.; Ward, B.; Williams, R.; Follows, M. The Impact of Fine-Scale Turbulence on Phytoplankton Community Structure. *Limnol. Oceanogr. Fluids Environ.* **2014**, *4*, 34–49. [CrossRef]
29. Wheeler, J.; Secchi, E.; Rusconi, R.; Stocker, R. Not Just Going with the Flow: The Effects of Fluid Flow on Bacteria and Plankton. *Annu. Rev. Cell Dev. Biol.* **2019**, *35*, 1–25. [CrossRef]
30. Pingree, R.; Holligan, P.; Mardell, G.; Head, R. The Influence of Physical Stability on Spring, Summer and Autumn Phytoplankton Blooms in the Celtic Sea. *J. Mar. Biol. Assoc. United Kingd.* **1976**, *56*, 845–873. [CrossRef]
31. Wihsgott, J.; Sharples, J.; Hopkins, J.; Woodward, E.; Hull, T.; Greenwood, N.; Sivyer, D. Observations of Vertical Mixing in Autumn and Its Effect on the Autumn Phytoplankton Bloom. *Prog. Oceanogr.* **2019**, *177*, 102059. [CrossRef]
32. Osborn, T. Finestructure, Microstructure, and Thin Layers. *Oceanography* **1998**, *11*, 36–43. [CrossRef]
33. Lueck, R.; Wolk, F.; Yamazaki, H. Oceanic Velocity Microstructure Measurements in the 20th Century. *J. Phys. Oceanogr.* **2002**, *58*, 153–174. [CrossRef]
34. Shang, X.; Qi, Y.; Chen, G.; Liang, C.; Lueck, R.; Prairie, B.; Li, H. An Expendable Microstructure Profiler for Deep Ocean Measurements. *J. Atmos. Ocean. Technol.* **2016**, *34*, 153–165. [CrossRef]
35. van Haren, H. Internal Wave Mixing in Warming Lake Grevelingen. *Estuar. Coast. Shelf Sci.* **2019**, *226*, 106298. [CrossRef]
36. van Haren, H.; Piccolroaz, S.; Amadori, M.; Toffolon, M.; Dijkstra, H. Moored Observations of Turbulent Mixing Events in Deep Lake Garda, Italy: Mixing Events in Deep Lake Garda. *J. Limnol.* **2020**, *80*. [CrossRef]
37. Fernández-Castro, B.; Bouffard, D.; Troy, C.; Ulloa, H.; Piccolroaz, S.; Steiner, S.; Chmiel, H.; Moncadas, L.; Lavanchy, S.; Wuest, A. Seasonality Modulates Wind-Driven Mixing Pathways in a Large Lake. *Commun. Earth Environ.* **2021**, *2*, 215. [CrossRef]
38. Pearson, B.; Fox-Kemper, B. Log-Normal Turbulence Dissipation in Global Ocean Models. *Phys. Rev. Lett.* **2018**, *120*, 094501. [CrossRef] [PubMed]
39. Benway, H.M.; Lorenzoni, L.; White, A.E.; Fiedler, B.; Levine, N.M.; Nicholson, D.P.; DeGrandpre, M.D.; Sosik, H.M.; Church, M.J.; O'Brien, T.D.; et al. Ocean Time Series Observations of Changing Marine Ecosystems: An Era of Integration, Synthesis, and Societal Applications. *Front. Mar. Sci.* **2019**, *6*, 393. [CrossRef]
40. Ribera d'Alcalà, M.; Conversano, F.; Corato, F.; Licandro, P.; Mangoni, O.; Marino, D.; Mazzocchi, M.G.; Modigh, M.; Montresor, M.; Nardella, M.; et al. Seasonal Patterns in Plankton Communities in Pluriannual Time Series at a Coastal Mediterranean Site (Gulf of Naples): An Attempt to Discern Recurrences and Trends. *Sci. Mar.* **2004**, *68*, 65–83. [CrossRef]
41. Zingone, A.; D'Alelio, D.; Mazzocchi, M.G.; Montresor, M.; Sarno, D. Time Series and Beyond: Multifaceted Plankton Research at a Marine Mediterranean LTER Site. *Nat. Conserv.* **2019**, *34*, 273–310. [CrossRef]
42. Piccolroaz, S.; Fernández-Castro, B.; Toffolon, M.; Dijkstra, H. A Multi-Site, Year-Round Turbulence Microstructure Atlas for the Deep Perialpine Lake Garda. *Sci. Data* **2021**, *8*, 188. [CrossRef]
43. Ferron, B.; Aubertot, P.B.; Cuypers, Y.; Vic, C. Removing Biases in Oceanic Turbulent Kinetic Energy Dissipation Rate Estimated from Microstructure Shear Data. *J. Atmos. Ocean. Technol.* **2023**, *40*, 129–139. [CrossRef]
44. Lueck, R. *RSI Technical Note 028: Calculating the Rate of Dissipation of Turbulent Kinetic Energy*; Rockland Scientific International Inc.: Victoria, BC, Canada, 2016.
45. Goodman, L.; Levine, E.R.; Lueck, R.G. On Measuring the Terms of the Turbulent Kinetic Energy Budget from an AUV. *J. Atmos. Ocean. Technol.* **2006**, *23*, 977–990. [CrossRef]
46. Lueck, R.; MacIntyre, D.; McMillan, J. *RSI Technical Note 061: Goodman Coherent Noise Removal—Spectral Bias*; Rockland Scientific International Inc.: Victoria, BC, Canada, 2022.
47. Nuttall, A.H. Spectral Estimation by Means of Overlapped Fast Fourier Transform Processing of Windowed Data. NUSC Tech. Rep. No. 4169 1971. Available online: https://apps.dtic.mil/sti/citations/AD0739315 (accessed on 14 February 2023).
48. Ruddick, B.; Anis, A.; Thompson, K. Maximum Likelihood Spectral Fitting: The Batchelor Spectrum. *J. Atmos. Ocean. Technol.* **2000**, *17*, 1541–1555. [CrossRef]
49. Hebert, D.A.; de Bruyn Kops, S.M. Predicting Turbulence in Flows with Strong Stable Stratification. *Phys. Fluids* **2006**, *18*, 066602. [CrossRef]
50. Schultze, L.; Merckelbach, L.; Carpenter, J. Turbulence and Mixing in a Shallow Shelf Sea from Underwater Gliders. *J. Geophys. Res. Ocean.* **2017**, *122*, 9092–9109. [CrossRef]

51. Gregg, M. Diapycnal Mixing in the Thermocline: A Review. *J. Geophys. Res.* **1987**, *92*, 5249–5286. [CrossRef]
52. Shih, L.; Koseff, J.; Ivey, G. Parameterisation of Turbulent Fluxes and Scales Using Homogeneous Sheard Stratified Turbulence Simulations. *J. Fluid Mech.* **2005**, *525*, 193–214. [CrossRef]
53. Ivey, G.; Winters, K.B.; Koseff, J. Density Stratification, Turbulence, but How Much Mixing? *Annu. Rev. Fluid Mech.* **2008**, *40*, 169–184. [CrossRef]
54. Bouffard, D.; Boegman, L. A Diapycnal Diffusivity Model for Stratified Environmental Flows. *Dyn. Atmos. Ocean.* **2013**, *61–62*, 14–34. [CrossRef]
55. McDougall, T.J.; Barker, P.M. Getting Started with TEOS-10 and the Gibbs Seawater (GSW) Oceanographic Toolbox. *SCOR/IAPSO WG* **2011**, *127*, 1–28.
56. Wolk, F.; Yamazaki, H.; Seuront, L.; Lueck, R. A New Free-Fall Profiler for Measuring Biophysical Microstructure. *J. Atmos. Ocean. Technol.* **2002**, *19*, 780–793. [CrossRef]
57. Copernicus Climate Change Service Climate Data Store (CDS). Copernicus Climate Change Service ERA5: Fifth Generation of ECMWF Atmospheric Reanalyses of the Global Climate. 2017. Available online: https://cds.climate.copernicus.eu/cdsapp#!/home (accessed on 6 July 2022).
58. Zhang, H.-M.; Talley, L. Heat and Buoyancy Budgets and Mixing Rates in the Upper Thermocline of the Indian and Global Oceans. *J. Phys. Oceanogr.* **1998**, *28*, 1961–1978. [CrossRef]
59. Large, W.G.; Pond, S. Open Ocean Momentum Flux Measurement in Moderate to Strong Winds. *J. Phys. Oceanogr.* **1981**, *11*, 336–342. [CrossRef]
60. Leibovich, S. The Form and Dynamics of Langmuir Circulations. *Annu. Rev. Fluid Mech.* **1983**, *15*, 391–427. [CrossRef]
61. Thorpe, S.A. Langmuir Circulation. *Annu. Rev. Fluid Mech.* **2004**, *36*, 55–79. [CrossRef]
62. Belcher, S.E.; Grant, A.; Hanley, K.; Fox-Kemper, B.; Roekel, V.; Sullivan, P.; Large, W.; Brown, A.; Hines, A.; Calvert, D.; et al. A Global Perspective on Langmuir Turbulence in the Ocean Surface Boundary Layer. *Geophys. Res. Lett.* **2012**, *39*, 9. [CrossRef]
63. Ardhuin, F.; Marié, L.; Rascle, N.; Forget, P.; Roland, A. Observation and Estimation of Lagrangian, Stokes, and Eulerian Currents Induced by Wind and Waves at the Sea Surface. *J. Phys. Oceanogr.* **2009**, *39*, 2820. [CrossRef]
64. Sayol, J.; Orfila, A.; Oey, L.-Y. Wind Induced Energy-Momentum Distribution along the Ekman-Stokes Layer. Application to the Western Mediterranean Sea Climate. *Deep Sea Res. Part I Oceanogr. Res. Pap.* **2016**, *111*, 34–49. [CrossRef]
65. Albanese, S.; Iavazzo, P.; Adamo, P.; Lima, A.; Vivo, D. Assessment of the Environmental Conditions of the Sarno River Basin (South Italy): A Stream Sediment Approach. *Environ. Geochem. Health* **2013**, *35*, 283–297. [CrossRef] [PubMed]
66. de Boyer Montégut, C.; Madec, G.; Fischer, A.; Lazar, A.; Iudicone, D. Mixed Layer Depth over the Global Ocean: An Examination of Profile Data and Profile-Based Climatology. *J. Geophys. Res.* **2004**, *109*, C12003. [CrossRef]
67. Klink, J. Dynmodes.m—Ocean Dynamic Vertical Modes. Woods Hole (MA): Woods Hole Science Center—SEA—MAT—Matlab Tools for Oceanographic Analysis. 1999. Available online: http://woodshole.er.usgs.gov/operations/sea-mat/index.html (accessed on 6 July 2019).
68. Lozovatsky, I.; Figueroa, M.; Roget, E.; Fernando, H.; Shapovalov, S. Observations and Scaling of the Upper Mixed Layer in the North Atlantic. *J. Geophys. Res.* **2005**, *110*. [CrossRef]
69. Visbeck, M.; Marshall, J.; Jones, H. Dynamics of Isolated Convective Regions in the Ocean. *J. Phys. Oceanogr.* **1996**, *26*, 1721–1734. [CrossRef]
70. Grant, A.; Belcher, S.E. Characteristics of Langmuir Turbulence in the Ocean Mixed Layer. *J. Phys. Oceanogr.* **2009**, *39*, 1871–1887. [CrossRef]
71. Moeng, C.-H.; Sullivan, P. A Comparison of Shear- and Buoyancy-Driven Planetary Boundary Layer Flows. *J. Atm. Sci* **1994**, *51*, 999–1022. [CrossRef]
72. Virtanen, P.; Gommers, R.; Oliphant, T.E.; Haberland, M.; Reddy, T.; Cournapeau, D.; Burovski, E.; Peterson, P.; Weckesser, W.; Bright, J.; et al. SciPy 1.0: Fundamental Algorithms for Scientific Computing in Python. *Nat. Methods* **2020**, *17*, 261–272. [CrossRef]
73. Burr, I. Cumulative Frequency Functions. *Ann. Math. Stat.* **1942**, *13*, 215–232. [CrossRef]
74. Lorbacher, K.; Dommenget, D.; Niiler, P.; Köhl, A. Ocean Mixed Layer Depth: A Subsurface Proxy of Ocean-Atmosphere Variability. *J. Geophys. Res. Ocean.* **2006**, *111*. [CrossRef]
75. Giunta, V.; Ward, B. Ocean Mixed Layer Depth from Dissipation. *J. Geophys. Res. Ocean.* **2022**, *127*, e2021JC017904. [CrossRef]
76. Osborn, T. Estimates of the Local Rate of Vertical Diffusion from Dissipation Measurements. *J. Phys. Oceanogr.* **1980**, *10*, 83–89. [CrossRef]
77. Kokoszka, F.; Iudicone, D.; Zingone, A.; Saggiomo, V.; Ribera d'Alcalà, M.; Conversano, F. A Note about Density Staircases in the Gulf of Naples: 20 Years of Persistent Weak Salt-Fingering Layers in a Coastal Area. *Adv. Oceanogr. Limnol.* **2021**, *12*. [CrossRef]
78. López-Tarazón, J.A.; Batalla, R.J.; Vericat, D.; Balasch, J. Rainfall, Runoff and Sediment Transport Relations in a Mesoscale Mountainous Catchment: The River Isábena (Ebro Basin). *Catena* **2010**, *82*, 23–34. [CrossRef]
79. Iermano, I.; Liguori, G.; Iudicone, D.; Nardelli, B.; Colella, S.; Zingone, A.; Saggiomo, V. Dynamics of Short-Living Filaments and Their Relationship with Intense Rainfall Events and River Flows. Available online: https://ui.adsabs.harvard.edu/abs/2009EGUGA..11.8508I/abstract (accessed on 6 July 2022).
80. Lozovatsky, I.; Fernando, H.J.S.; Planella-Morato, J.; Liu, Z.; Lee, J.-H.; Jinadasa, S.U.P. Probability Distribution of Turbulent Kinetic Energy Dissipation Rate in Ocean: Observations and Approximations. *J. Geophys. Res.* **2017**, *122*, 8293–8308. [CrossRef]

81. Buckingham, C.E.; Lucas, N.S.; Belcher, S.E.; Rippeth, T.P.; Grant, A.L.M.; Le Sommer, J.; Ajayi, A.O.; Naveira Garabato, A.C. The Contribution of Surface and Submesoscale Processes to Turbulence in the Open Ocean Surfaceboundary Layer. *J. Adv. Model. Earth Syst.* **2019**, *11*, 4066–4099. [CrossRef]
82. Cimatoribus, A.; Lemmin, U.; Bouffard, D.; Barry, D. Nonlinear Dynamics of the Nearshore Boundary Layer of a Large Lake (Lake Geneva). *J. Geophys. Res. Ocean.* **2018**, *123*, 1016–1031. [CrossRef]
83. Gallerano, F.; Cannata, G.; Palleschi, F. Nonlinear Waves and Nearshore Currents over Variable Bathymetry in Curve-Shaped Coastal Areas. *J. Ocean Eng. Mar. Energy* **2019**, *5*, 419–431. [CrossRef]
84. Masunaga, E.; Homma, H.; Yamazaki, H.; Fringer, O.; Nagai, T.; Kitade, Y.; Okayasu, A. Mixing and Sediment Resuspension Associated with Internal Bores in a Shallow Bay. *Cont. Shelf Res.* **2015**, *110*, 85–99. [CrossRef]
85. van Haren, H.; Duineveld, G.; Mienis, F. Internal Wave Observations off Saba Bank. *Front. Mar. Sci.* **2019**, *5*. [CrossRef]
86. Green, M.; Coco, G. Review of Wave-Driven Sediment Resuspension and Transport in Estuaries. *Rev. Geophys.* **2014**, *52*, 77–117. [CrossRef]
87. Sutherland, G.; Christensen, K.; Ward, B. Evaluating Langmuir Turbulence in the Oceanic Boundary Layer. *J. Geophys. Res. Ocean.* **2014**, *119*, 1899–1910. [CrossRef]
88. Qiu, C.; Dan, H.; Changjian, L.; Cui, Y.; Su, D.; Wu, J.; Juan, O. Upper Vertical Structures and Mixed Layer Depth in the Shelf of the Northern South China Sea. *Cont. Shelf Res.* **2019**, *174*, 26–34. [CrossRef]
89. Taylor, J.; Ferrari, R. Buoyancy and Wind-Driven Convection at Mixed Layer Density Fronts. *J. Phys. Oceanogr.* **2010**, *40*, 1222–1242. [CrossRef]
90. Polton, J.; Smith, J.; Mackinnon, J.; Tejada-Martínez, A. Rapid Generation of High-Frequency Internal Waves beneath a Wind and Wave Forced Oceanic Surface Mixed Layer. *Geophys. Res. Lett.* **2008**, *35*. [CrossRef]
91. Kelly, S. Coastally Generated Near-Inertial Waves. *J. Phys. Oceanogr.* **2019**, *49*, 2979–2995. [CrossRef]
92. Burchard, H.; Rippeth, T. Generation of Bulk Shear Spikes in Shallow Stratified Tidal Seas. *J. Phys. Oceanogr.* **2009**, *39*, 969–985. [CrossRef]
93. Lincoln, B.; Rippeth, T.; Simpson, J. Surface Mixed Layer Deepening through Wind Shear Alignment in a Seasonally Stratified Shallow Sea. *J. Geophys. Res. Ocean.* **2016**, *121*, 6021–6034. [CrossRef]
94. Xie, X.; Li, M. Generation of Internal Lee Waves by Lateral Circulation in a Coastal Plain Estuary. *J. Phys. Oceanogr.* **2019**, *49*, 1687–1697. [CrossRef]
95. Passaro, S.; Tamburrino, S.; Vallefuoco, M.; Gherardi, S.; Sacchi, M.; Guido, V. High-Resolution Morpho-Bathymetry of the Gulf of Naples, Eastern Tyrrhenian Sea. *J. Maps* **2016**, *12*, 203–210. [CrossRef]
96. Ruggiero, P.; Ernesto, N.; Iacono, R.; Pierini, S.; Spezie, G. A Baroclinic Coastal Trapped Wave Event in the Gulf of Naples (Tyrrhenian Sea). *Ocean Dyn.* **2018**, *68*, 1683–1694. [CrossRef]
97. Pinkel, R.; Goldin, M.; Smith, J.; Sun, O.; Aja, A.; Bui, M.; Hughen, T. The Wirewalker: A Vertically Profiling Instrument Carrier Powered by Ocean Waves. *J. Atmos. Ocean. Technol.* **2011**, *28*, 426–435. [CrossRef]
98. Le Boyer, A.; Alford, M.; Couto, N.; Goldin, M.; Lastuka, S.; Goheen, S.; Nguyen, S.; Lucas, A.; Hennon, T. Modular, Flexible, Low-Cost Microstructure Measurements: The Epsilometer. *J. Atmos. Ocean. Technol.* **2021**, *38*, 657–668. [CrossRef]
99. Roemmich, D.; Alford, M.; Claustre, H.; Johnson, K.; King, B.; Moum, J.; Oke, P.; Owens, W.; Pouliquen, S.; Purkey, S.; et al. On the Future of Argo: A Global, Full-Depth, Multi-Disciplinary Array. *Front. Mar. Sci.* **2019**, *6*. [CrossRef]
100. Somavilla, R.; Gonzalez-Pola, C.; Fernandez-Diaz, J. The Warmer the Ocean Surface, the Shallower the Mixed Layer. How Much of This Is True? *J. Geophys. Res.* **2017**, *122*, 7698–7716. [CrossRef] [PubMed]
101. Guancheng, L.; Cheng, L.; Zhu, J.; Trenberth, K.; Mann, M.; Abraham, J. Increasing Ocean Stratification over the Past Half-Century. *Nat. Clim. Chang.* **2020**, *10*, 1116–1123. [CrossRef]